Seabed Structure Inferences From TREX13 Reflection Measurements

Charles W. Holland, Samuel Pinson, Chad M. Smith, *Member, IEEE*, Paul C. Hines, Derek R. Olson,
Stan E. Dosso, and Jan Dettmer

Abstract—Seabed reflection measurements can be used to infer highly detailed properties of marine sediments. The information content is largely contained in the interference pattern in frequency-angle arising from wave constructive and destructive interference in a plane layer. Wide-angle reflection measurements at a ridge crest and a swale site off the coast of Panama City, FL, USA, instead show interference patterns that are highly perturbed. Interface roughness was hypothesized to be the cause of the perturbations. This hypothesis is examined using numerical simulations. Measured data and simulations at the swale site show broadband peaks and troughs due to focusing/defocusing effects from boundary curvature which perturbs the interference pattern. While the hypothesis roughness is likely correct at the swale site, the roughness statistics are not known sufficiently to validate the hypothesis. At the crest site including roughness did not lead to strong similarities with the data. Interference pattern perturbations at both sites eliminated the possibility of estimating sediment parameters from inversion of broadband wide-angle data. Instead, sediment properties were estimated by inspection and forward modeling. The estimates reasonably agree with geoacoustic properties estimated from normal incidence measurements in the swale and indicate similar sound speeds and densities on two ridges ∼6 km apart.

Index Terms—Geoacoustic properties, roughness, seabed reflection.

I. Introduction

MIDFREQUENCY 1–10-kHz reverberation in littoral regions is often controlled by seabed mechanisms. For example, in isospeed or downward refracting conditions, seabed properties often dominate boundary reflection and scattering, which are both important factors for reverberation. Seabed reflection is often approximated (modeled) using flat boundaries and bulk sediment properties, i.e., smoothly varying properties within a sediment layer, and ignoring heterogeneities or fluctuations, e.g., [1]. Seabed scattering, on the other hand, is a function of both of the smoothly varying sediment properties and small-scale inhomogeneities, e.g., [2].

The bulk sediment properties of interest are the compressional wave speed and attenuation and density as a function of depth and frequency. Measurement of even these properties (under the fluid sediment approximation) is challenging. There are a number of approaches for measuring these properties including direct (e.g., coring) and remote sensing or geoacoustic inversion approaches (e.g., sediment property inference from acoustic measurements), each of which has advantages and disadvantages.

The observational approach here employs measurements of broadband wide-angle seabed reflection. The advantages of this approach are:

1) high resolution vertically, 0.1 m and laterally, $O(10^1)$m;
2) relatively small uncertainties from the space/time-varying oceanography and biologics due to short path lengths;
3) low source levels are possible;
4) the data are expected to be highly informative for seabed geoacoustic properties, especially sound speed, density, and attenuation dependencies on depth and frequency (e.g., see [3]).

Wide-angle reflection measurements can be conducted with a moving source and receiver to probe lateral variability (e.g., [4]); however in this experiment, the receiver was fixed. To probe lateral variability, broadband normal incidence reflection data were also measured. These data have significantly lower information content than the wide-angle data, and lead to numerous parameter ambiguities in estimating sediment properties. Nevertheless, these data can be useful for developing a broad understanding of the sediment spatial variability.

The high information content of the wide-angle reflection data is primarily contained in the interference pattern across frequency and angle caused by a layered medium. The interference pattern is due to the classical quarter-wavelength and half-wavelength resonances in a given layer that lead to nulls and peaks, respectively, in the reflection coefficient across frequency and angle. The interference pattern has always been observed in dozens of our previous wide-angle measurements. Its presence has opened the door to estimating: layer thicknesses [5], the number of layers[1] [6], density gradients [7], sound speed, and attenuation dispersion [3] (i.e., their frequency dependence

---

[1]In most geoacoustic inversion approaches, the number of layers must be chosen by the researcher before performing the inversion, but broadband wide-angle reflection data contain sufficient information through the interference pattern to permit number of layers itself to be a parameter determined by the data; see [6].

which is typically difficult to obtain), and spatial variability (e.g., [4] and [8]).

All of these previous measurements were conducted on the mid to outer shelf, in water depths 80–180 m. This experiment was sited in a water depth of 20 m off Panama City, FL, USA, as part of the 2013 Target and Reverberation Experiment (TREX13). In this inner shelf region, there is significantly more wind, wave, and current energy at the benthic boundary. This, coupled with proximity to varied sediment fabrics, e.g., estuarine and marine, leads to much higher geoacoustic spatial variability (including larger interface roughness and stronger sediment volume heterogeneities) than on mid to outer shelf regions. Thus, our past assumption of flat interfaces and no significant sediment heterogeneities turned out to be inappropriate for this environment.

The paper is organized as follows. In Section II, the design of the reflection experiment is discussed. Wide-angle data processing is described and the reflection data are presented in Section III. Modeling and inspection of the data indicate that the interference pattern has been perturbed, which prevents statistical inference using a plane-layered model. Instead, geoacoustic properties are estimated from the wide-angle data using theory and forward modeling. One cause of the perturbations is hypothesized to be layer roughness and this hypothesis is explored by numerical simulations at both the ridge crest site and the swale site. In Section IV, normal incidence seabed reflection data are presented and analyzed near the swale site and the estimated geoacoustic properties are compared with those estimated from wide-angle data. Section V presents the conclusions and summary.

II. Measurement Design

The goal of the seabed reflection measurements was to provide bulk sediment properties in each sediment layer. This is required for 1) modeling scattering, which requires an understanding of the background medium (scattering data generally contain insufficient information content to obtain both the background and the fluctuating components); and 2) modeling propagation.

One of the experimental challenges of wide-angle measurements is multipath separation, in particular separation of the direct path, the seabed reflected path, and sea surface reflected path. At the TREX13 location, the 20-m water depth and the inability to employ a source very near the sea surface (the usual geometry) necessitated a particularly precise design of the geometry and waveforms.

The experiment design is shown in Fig. 1, where a small, $\sim 1 \times 2$ m, catamaran was deployed about 20 m aft of Canadian Forces Auxiliary Vessel *Quest*. The source was suspended below the catamaran 7–10 m, depending on the run. To limit the vertical and horizontal displacement of the source due to drag, a line was connected from the tow cable to the suspension line just above a 10-kg weight (not shown) several meters below the catamaran. The source was an ITC-1007 spherical transducer which transmitted an equalized 0.25-s linear frequency modulated (LFM) down sweep from 12 to 1.4 kHz at
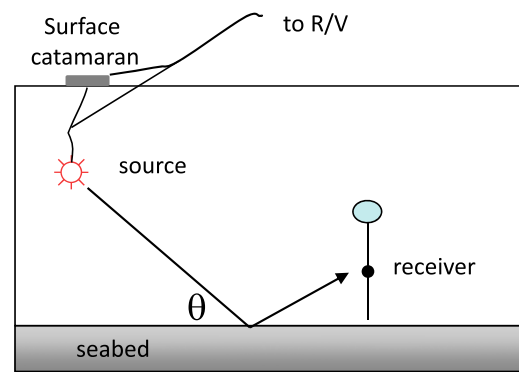

Fig. 1. Experiment design. The water depth is about 20 m; source and receiver depths were about 7 and 16 m, respectively. A reference hydrophone (not shown) 2 m above the source served to monitor source transmissions as well as measuring normal incidence reflections from the seabed.

160 dB re 1 μPa @ 1 m and a repetition rate of 0.5 s. A depth sensor and reference hydrophone were placed about 1 and 2 m above the source, respectively. The reference hydrophone was employed both to monitor the source transmission and to measure normal incidence reflection.

The receiver consisted of three self-recording hydrophones placed along a vertical mooring line 7.5 m in length with a 0.25-m radius float providing buoyancy at the top. Signals from two hydrophones were slightly contaminated by scattering from corners and edges of the small potted rectangular electronics boxes which were within ~ 0.1 m of the hydrophone. The third hydrophone (icListen HF) deployed at ~ 16-m depth exhibited a clean signal and was used in this analysis. The receiver dynamic range was 120 dB and the sampling rate 64 kHz.

The ship transited as slowly as practical, given the sea conditions, while maintaining navigation along a straight line. Typically the speed was about 1.5 m/s. To achieve the widest possible angular coverage, the tracks were planned such that the catamaran transited directly over the receivers. Despite difficulties attendant to low-speed navigation and position uncertainties of the source and receiver, the minimum horizontal distance between source and receiver was typically about 10 m (estimated by geometry reconstruction discussed later). The very close proximity of the ship to the receiver required low ship radiated noise levels, which was achieved. There were also concerns in the planning stage about reflections from the ship hull, which were indeed observed in the measured data when approaching the receiver. However, hull reflections were sufficiently separated in time from the seabed arrivals that they did not affect the data processing.

Wide-angle seabed reflection measurements were conducted at two locations, see Fig. 2. The swale site is located between two small ridges near the end of the ridge-swale topography [9] and the ebb tide delta (bathymetric bulge) seen in the lower right-hand corner of Fig. 2. The sediments there are characterized by a poorly sorted conglomeration of sand and shells with a significant fine fraction [10]. In this area, it was difficult to map the mid-sand-sheet reflector beneath the poorly sorted sediment from the seismic data, but it was speculated to be about a meter or less below the seafloor [10]. The swale site is positioned slightly
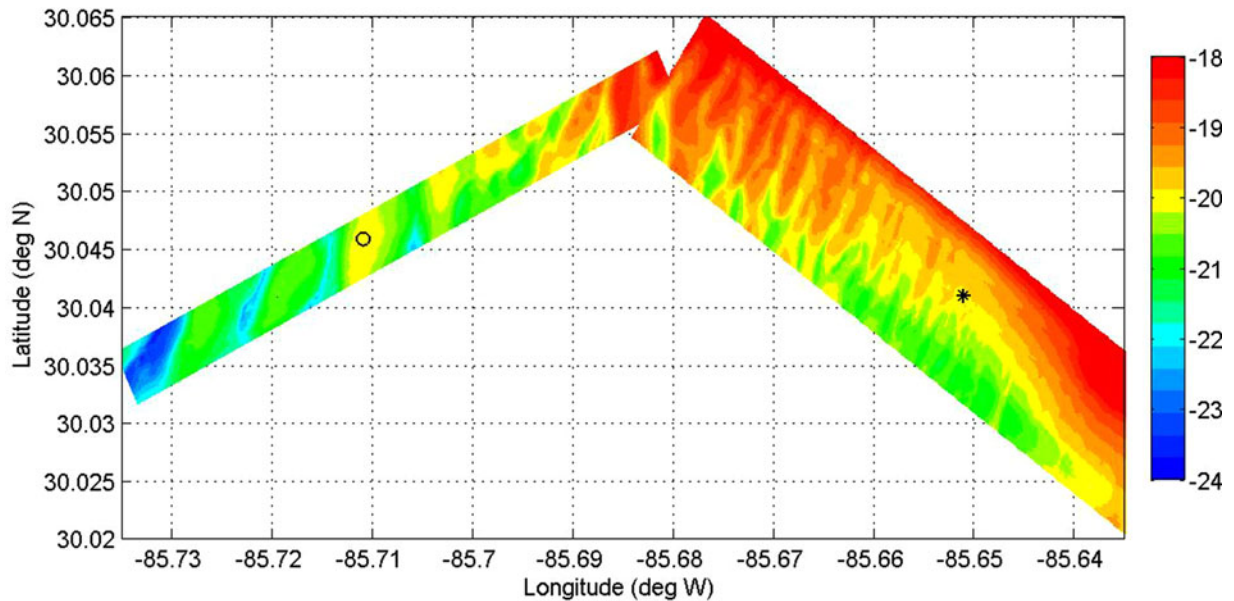
Fig. 2.   Bathymetry (in meters) and location of swale ($*$) and crest ($\circ$) reflection sites.

north Northeast of the main reverberation track center line. The second location, the crest site, was centered on a ridge crest along a different bearing. The measurements were conducted on May 3 (crest site) and May 5 (swale site) 2013; the sound-speed profiles at both sites were nearly isovelocity.

III. WIDE-ANGLE REFLECTION

A. Data Processing

The quantity of interest is the seabed spherical wave reflection coefficient. It is defined as the ratio of the reflected acoustic pressure at a given source–receiver position, scaled by Green's function for the specular path as if the seabed were a perfectly reflecting half-space (for details, see [11]). Two differences from the processing in [11] and this experiment are: 1) the necessity to account for the Doppler shift (prior measurements either used an impulsive source, or the source and receivers were moving in tandem); and 2) the necessity to estimate source–receiver offsets using relative travel time between the direct, bottom, and sea surface paths. Both of these are described below.

1) Doppler Estimation: The use of a broadband LFM signal from a moving source and fixed receiver necessitated Doppler compensation. The Doppler corrections are important for temporally separating the direct, bottom, and surface paths so that the reflection coefficient can be formed by scaled ratio of the bottom and direct path total energies. In cases where there is a sufficiently large temporal separation of the paths, e.g., high angles, there is no difference between Doppler-corrected and no Doppler-corrected reflection coefficients. That is, Doppler effects do not change the total energy.

While there was a global positioning system (GPS) unit on the catamaran, neither the source position (beneath the catamaran), nor the receiver position were precisely known. Doppler estimation is often performed using a search algorithm resulting

in an ambiguity function, from which the most likely Doppler speed is drawn. Pinson [12] developed a simpler method using the phase of the Doppler cross-power spectrum that performed as well or better than the search method on these datasets. Examples of the results are shown in Fig. 3, where the "raw" curve (blue line) represents match-filtering with the transmitted pulse. The curve labeled "Dop compen" (red line) represents match-filtering with Doppler compensation applied to the transmitted pulse. The first arrival is the direct path. Note that in the raw match-filtered data, the low frequencies arrive first/last on the incoming/outgoing legs. The Doppler processing properly compensates for the relative motion, shortening the width and increasing the peak of the direct path arrival. Near the closest point of approach (CPA), the effect of the Doppler shift is small, as expected. The estimated relative speeds from the Doppler processing agrees closely with the measured speed from a GPS unit mounted on the catamaran, which gives confidence in the method (see Appendix 1, Fig. 18).

Doppler estimation was performed on the direct path only and the Doppler compensation was applied to the entire signal. While the Doppler shift for the bottom reflected path will differ from that of the direct path, the difference is expected to be very small because the receiver is only a few meters above the seabed, i.e., the path difference between the direct and bottom paths are relatively small. The effect of ignoring the slightly different Doppler is that the match-filtered data for the bottom reflected path will have a slightly lower and broader peak than for perfect compensation. Since the wide-angle reflection processing is based on waveform energy, not peak amplitude (i.e., the time series are integrated across separate time windows containing the direct and bottom reflected paths), the slight mismatch will not lead to errors in the magnitude of the reflection coefficient. There will be a slight shift in the spectrum, but this is expected to be negligible for the 50-Hz processing bandwidth.
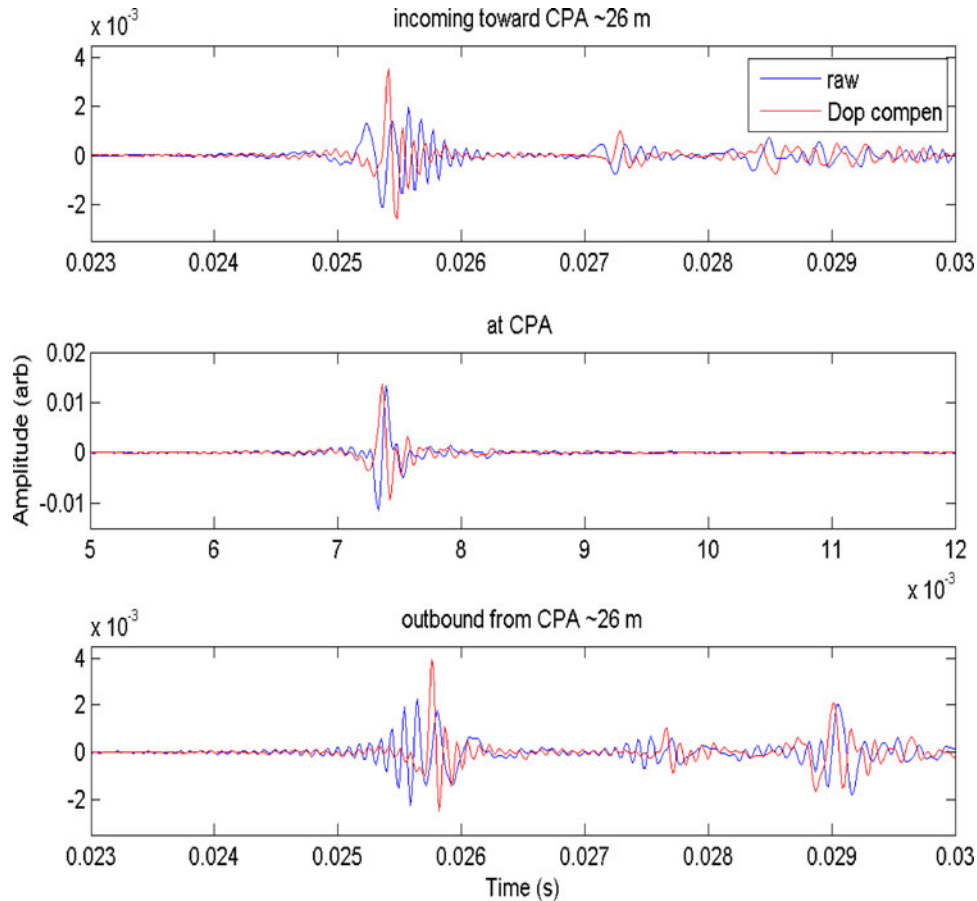
Fig. 3. Example of raw data using the transmitted waveform as the replica (blue) and the Doppler compensated pulse (red) at three source-receiver offsets: 26 m incoming, near the CPA, and 26 m outbound.

The Doppler corrected time series data, Fig. 4, show the direct path (first arrival), followed by the seabed reflected arrival, followed by the sea surface arrival (expressions of individual waves can be observed). Since the clock drift on the self-recording receiver was unknown, the transmitted source pulse arrival time is not known at this stage of the analysis. Even relative time (i.e., picking an arbitrary transmit time) was useful since in the initial analysis the slope of the incoming and outgoing direct path arrivals differed by a factor of 2. For the nearly constant ship speed, the slopes should be nearly identical. The slope differences meant that there was a 16.4-Hz error in the nominal sampling frequency of the transmitted pulse (which was later verified). In this plot, the correct sampling frequency has been used.

To determine arrival times, or equivalently the source–receiver offsets, an inversion method was employed using travel time differences between the direct, bottom, and sea surface paths (see Appendix 1).

2) Reflection Data Processing: Given source–receiver horizontal offsets or ranges r, the data can be examined in reduced time, $\tau = (t^2 - (r/c_{\rm red})^2)^{1/2}$ where t is time, $c_{\rm red}$ is an arbitrary reducing velocity, here $c_{\rm red} = c_w = 1524$ m/s where c_w is the seawater sound speed. This essentially removes the hyperbolae relating range offset with arrival time, flattening out the arrival times, see Fig. 5. The first arrival in Fig. 5 is the direct path; the second arrival is the seabed reflected path. Each trace

represents a different seabed angle and thus each angle samples a slightly different portion of the seabed. From a ray point of view, the specularly reflected ray strikes the seabed 3.5/14 m from the receiver at the steepest/shallowest angle. The spatial dimension of the insonified region around each seabed specular point is defined by the Fresnel zone, which is an ellipse. The major axis of the ellipse is along the line connecting source and receiver projected on the seabed (termed "in-plane"), and the minor axis is perpendicular. For example at 2 kHz, the in-plane Fresnel radius is 11 m at the lowest angle and 1.5 m at the steepest angle. Given the high pulse repetition rate and low source speed, substantial overlap of the insonified area exists from angle to angle along the track. The total in-plane region of seabed that is probed in this geometry, including the Fresnel zone, is about 25 m, that is, 25 m on the incoming (negative ranges) and 25 m on the outgoing (positive ranges) tracks.

On the incoming track the multibeam data show a very slightly sloping seabed (less than 0.1°). The nearly flat nature of the seabed is borne out by inspection of the seabed reflected path (negative ranges) in Fig. 5, which is essentially constant in time. Note that on the outgoing leg, at ~58 m, arrival times indicate that the bathymetry has a slight change of slope.

The third arrival in Fig. 5 is the sea surface reflected path. The strong arrival time variation associated with this path is due to individual sea surface waves. The sea state during the
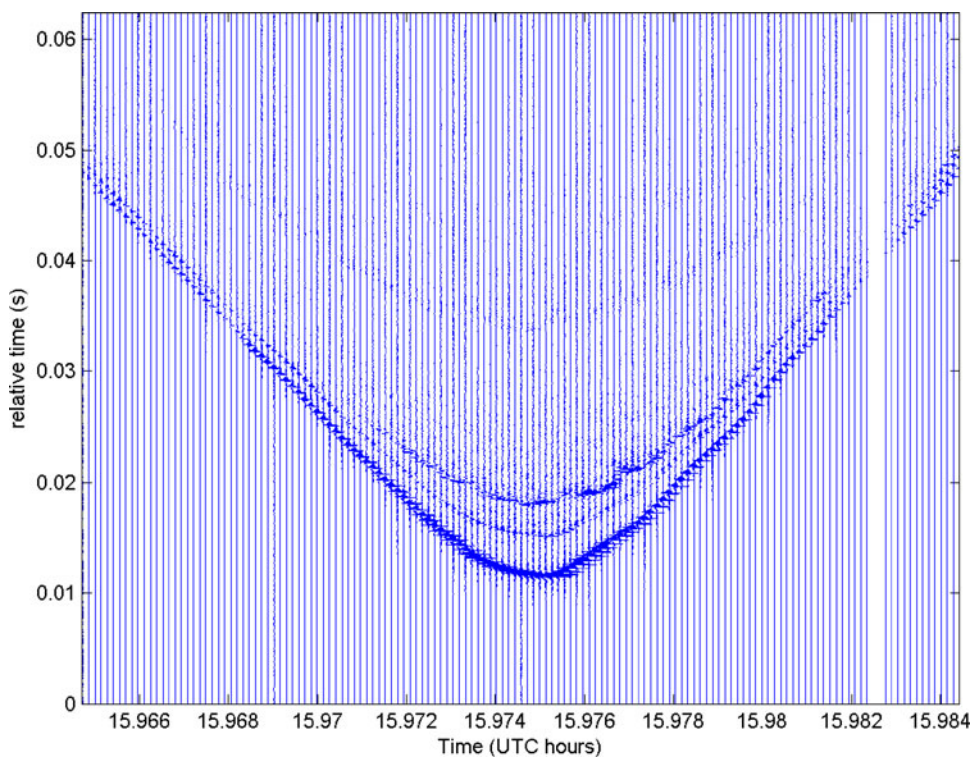
Fig. 4. Stacked pulse arrivals at the swale site. The arrival times are arbitrary, in the sense that the transmit time is not known at this stage of the processing.
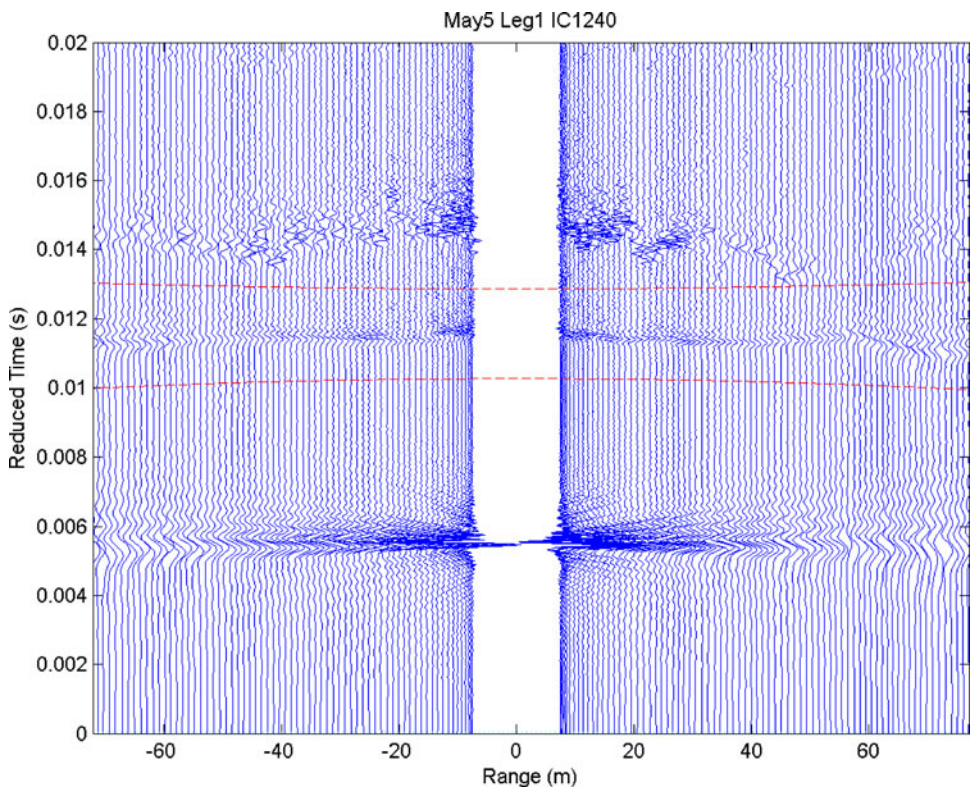

Fig. 5. Swale site measured data with Doppler corrections. The first arrival is the direct path, the second and third arrivals are the seabed and sea surface reflected arrivals, respectively. The red dashed lines show the temporal window used to estimate the seabed reflected pressure.
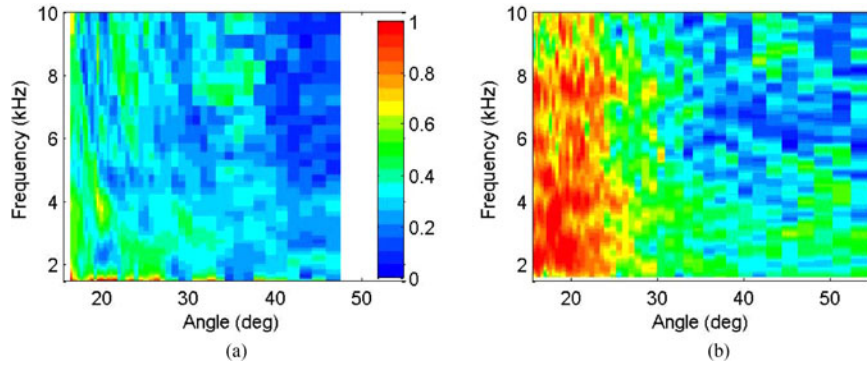
Fig. 6. Magnitude of the measured wide-angle pressure reflection coefficient at (a) swale site and (b) crest site. Note the significant difference in the reflection coefficient between the two sites indicating significant differences in seabed characteristics.

experiment increased rapidly with an incoming storm beginning with this leg. The red dashed line shows the time window used to estimate the seabed reflection coefficient. Only data from the incoming leg (negative ranges) were used for analysis, since the sea surface waves on the outgoing leg are sufficiently large to cause a leakage into the bottom reflection window at some ranges.

A window of the same size was formed around the direct path (not shown), and from data within these windows, the direct and seabed reflected pressures were estimated. The reflection coefficient is a scaled ratio of these quantities [11]. The resulting swale site reflection coefficient as a function of angle and frequency is shown in Fig. 6(a). Identical processing was performed at the crest site and the reflection coefficient is shown in Fig. 6(b). Note the significant differences between the reflection coefficients at the two sites, indicating substantial differences in seabed properties.

B. Geoacoustic Estimation and Hypothesis Testing

The goal of the analysis is to estimate seabed properties from the reflection data (Fig. 6). It is instructive to first perform some simple modeling to gain insight into the information content of the data.

1) Crest Site: At the crest site, there is a clear critical angle at, $\theta_c \sim 25°$; from Snell's law this means that the sediment sound speed is about $c_s = c_w/\cos(\theta_c) = 1680$ m/s. This is a value associated with a sandy sediment fabric. If it is first assumed that the sediment is a homogeneous half-space, density can be estimated from the reflection coefficient R at angles far above θ_c where, $\rho_s = \rho_w \, c_w/c_s(1 + R(\theta \gg \theta_c))/(1 - R(\theta \gg \theta_c)) \sim 1.9$ g/cm^3. This value is reasonably consistent with empirical relations, e.g., [13], given a sound speed of 1680 m/s.

A second assumption is made that the incident field can be approximated by plane waves. Then the parameters and the assumptions can be tested by comparing the measured data with the modeled plane-wave reflection coefficient, Fig. 7(a). Note that the gross features of the angular dependence are modeled, however, there are substantial differences. First, the reflection data show a much greater variability above the critical angle. Second, the angular dependence of the simulation near the
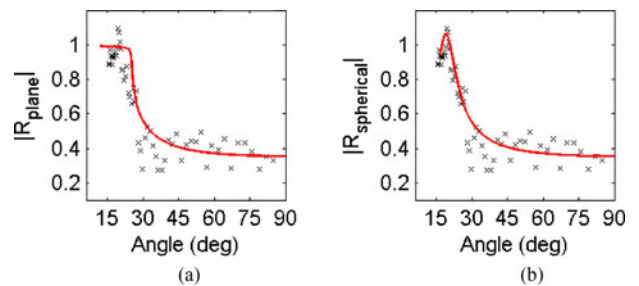

Fig. 7. Measured (x) 2 kHz pressure reflection coefficients at the crest site, and modeled results (line) assuming incident: (a) plane waves and (b) spherical waves. Note that near the critical angle, the spherical wave effects predict the data more closely. The geoacoustic parameters are given in Table I.

critical angle is not compelling. If spherical wavefronts are important, reflections at multiple angles contribute to a single reference angle, resulting in a reflection coefficient than can be greater than unity. Removing the plane wave assumption (i.e., performing the plane wave expansion for spherical waves from the source) yields the result in Fig. 7(b). Note that the behavior around the critical angle is more accurately modeled. This indicates that spherical wave effects are important for this experiment geometry and should be included. The peak in the measured and modeled data around 20° is due to the constructive interference between the classical reflected wave and the lateral wave.

It is useful at this stage to examine the forward model predictions across all frequencies. Fig. 8(d) shows the measured data in their full angular coverage. The increased dynamic range permits examination of reflection coefficients greater than unity; note especially the peak and valley structure below the critical angle that diminishes with increasing frequency. Fig. 8(a) shows the predicted angle and frequency dependence of the half-space case. The half-space assumption results differ from the measured data in the following ways.

1) Below the critical angle:
   a) the data show a "patchy" frequency dependence, whereas the model shows a smooth variation with frequency of the interference structure;
   b) the data show a general decrease in amplitude with increasing frequency, whereas the model predicts a nearly constant amplitude with frequency.
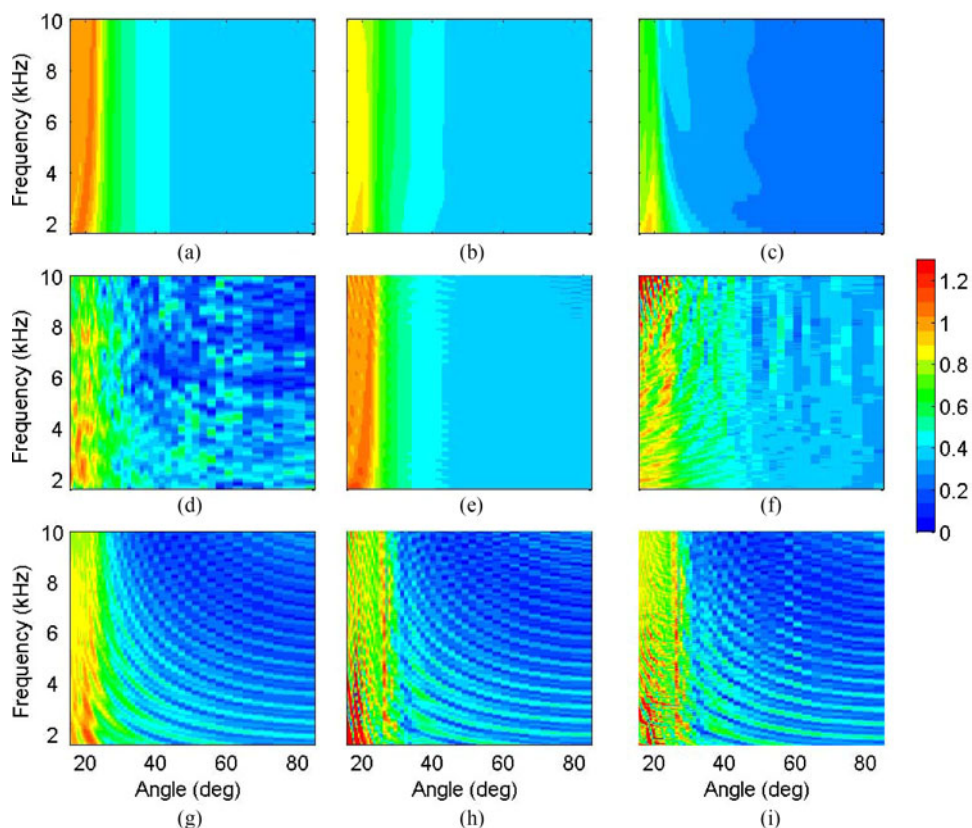
Fig. 8.   Crest site spherical reflection coefficients. The measured data are shown in (d). Modeled reflection coefficients from (a) homogeneous half-space, see Table I; (b) same parameters with linear attenuation profile from the sediment interface 0.8 to 0.1 dB/m/kHz at 0.4 m subbottom; (c) same parameters as (b) with a linear sound speed and density profile from 1600 m/s and 1.6 g/cm^3 at the water sediment interface to 1680 m/s and 1.9 g/cm^3 at 0.4 m subbottom; (e) homogeneous half-space with flat interface using the L–K model, (f) same as (e) but with roughness, Table IV laser line scanner parameters and $L = 0.2$ m, (g) layered seabed, see Table II; (h) layered seabed (L–K model) flat layers, (i) layered seabed (L–K model) with rough interfaces for the two lower layers only where w_1 is 5 and 10 times that of Table IV (multibeam) for the 4th and 5th interface, respectively, and $L = 2$ m.

2) The measured critical angle is nearly constant with frequency, perhaps decreasing at high frequencies (above 8 kHz), whereas the modeled critical angle increases with increasing frequency.

3) Above the critical angle:
   a) the data show a broad decrease in amplitude from low angles and low frequencies to high angles and high frequencies, while the model is independent of frequency;
   b) at a finer scale, the data show some evidence of layer interference and also several reflection coefficient highlights which are generally across a band of frequencies. The model results show no structure in angle-frequency space.

It is clear that the half-space model does not capture the measured data behavior and thus further modeling was performed with the goal of explaining that behavior.

Several hypotheses were explored to explain the angular and frequency dependence at and below the critical angle. One possible explanation for the decrease in the reflection coefficient with frequency below the critical angle is gradients in the geoacoustic properties. The effect of an attenuation gradient in the upper 0.4 m is shown in Fig. 8(b), which grossly shows the overall trend in the data both in terms of the decrease in amplitude and also

TABLE I
CREST SITE GEOACOUSTIC PARAMETERS FOR THE HOMOGENEOUS
HALF-SPACE SIMULATION

Sound speed (m/s)	Attenuation (dB/m/kHz)	Density (g/cm^3)
1680	0.05	1.9

The water sound speed is 1524 m/s. The attenuation is relatively poorly constrained.

the nearly uniform critical angle with frequency. The hypothesized negative attenuation gradient (decreasing attenuation with subbottom depth) could be due to increased overburden pressure and concomitant increase in grain-to-grain coupling. Such coupling would be expected to lead to positive gradients in sound speed and density. The effect of including sound speed, density, and attenuation gradients [see Fig. 8(c)] yields trends slightly more similar to the data. More sophisticated gradients (e.g., exponential) were briefly explored and gave similar results.

The frequency dependent behavior of the data below the critical angle [see Fig. 8(d)] and its nonuniform angular and frequency dependence above the critical angle [see Figs. 7(b) and 8(d)] both suggest that sediment layering may be present. A hypothesized four-layer seabed (see Table II) yields the reflection

Thickness (m)	Sound speed (m/s)	Attenuation (dB/m/kHz)	Density (g/cm^3)
0.01	1680	0.8	1.9
0.04	1555	0.6	1.6
1.5	1680	0.15	1.9
1.4	1555	0.1	1.6
–	1680	0.05	1.9

The water sound speed is 1524 m/s.

simulation shown in Fig. 8(g). The layered simulation mimics the data behavior much better below the critical angle, capturing both the "patchy" behavior with frequency and the diminishing amplitude as frequency increases. The layered simulation also captures the near frequency independence of the critical angle. At angles above the critical angle, the simulation captures the broad decrease in amplitude from low angles/frequencies to high angles/frequencies much better than the other models. Also, the evolution of the simulated interference pattern over angle and frequency is similar to that of the data between 30°–60° and 3–10 kHz, though the data show fewer and weaker interferences. It seems plausible that some mechanism has highly perturbed their structure. That is, the simulation has a much more regular structure than the data and does not capture the "highlights" that persist across frequency in the measured data.

Important aspects of the layered simulation [see Fig. 8(g)] include the presence of two identical intercalating sediment layers,[2] and an attenuation gradient with depth (from layer to layer). The layered model is speculative. From a geologic process point of view, it is not clear how sediment layers with a nonnegligible fine-grained component would be present on the ridge crest, but this could be possible from a large storm or hurricane. If such a process did occur, multiple events at different times creating multiple layers would be plausible. Other hypotheses, interface and subbottom roughness, Fig. 8(f) and (i), respectively, will be discussed at a later point (end of Section III).

The modeling here assumes that the sound speed in a given layer is independent of frequency, i.e., no dispersion. This assumption can be examined by inspection of the frequency dependence of the critical angle in Fig. 8. First note that with spherical wave effects, the critical angle increases with increasing frequency due the reduction in Fresnel zone size (and associated averaging over vertical angle). This can clearly be seen in Fig. 8(a) with no dispersion. If positive dispersions (an increase in sound speed with frequency) were present, this would lead to an even greater increase in the critical angle with increasing frequency. However, the data [see Fig. 8(d)] indicate that there is no substantial change in the critical angle with increasing frequency. Thus, with the homogeneous half-space assumption, to fit the frequency dependence of the observed critical angle, negative dispersion (decreasing sound speed with increasing

frequency) must be invoked. Negative dispersion can only be invoked when many large scatterers are present of the order of or greater than the wavelength. While shells and shell fragments do exist in the sediment, their size is much smaller than what would produce negative dispersion.[3]

Since the half-space assumption fails to explain the frequency dependence of the critical angle, some kind of structure in the seabed must be presumed. Here, two explanations for the critical angle frequency dependence are posited, gradients [see Fig. 8(b) and (c)] or layering [see Fig. 8(g)]. Either mechanism, or potentially both together, give a reasonable explanation for the frequency dependence of the critical angle.

The "perturbed" somewhat random pattern above the critical angle in the measured data was surprising inasmuch as extensive prior reflection measurements at other locations showed a clear interference pattern (as just one example, consider Fig 4(a) of [14]). Without the interference pattern, it seemed highly likely that inversions based on a plane-layered medium (e.g., [6]) would fail since this is clearly a poor approximation here. Nevertheless, for "completeness," a trans-dimensional Bayesian inversion was attempted, which resulted in an unsatisfactory half-space solution, similar to Fig. 8(a).

The observations at the ridge crest site are summarized as follows.

1) There is clear evidence that spherical wave effects are important, i.e., the presence of the interference structure below the critical angle caused by the lateral wave.
2) The frequency dependence of the observed critical angle:
   a) suggests weak or no sound speed dispersion from 1.5–10 kHz;
   b) cannot be explained by a homogeneous half-space, some kind of structure must be present;
   c) can be explained by layering.
3) The observations below the critical angle:
   a) cannot be explained by a homogeneous half-space, some kind of structure is present;
   b) suggests that layering is present, layering with gradients in sound speed, density, and attenuation is also plausible.
4) The observations above the critical angle:
   a) do not support a homogeneous half-space model. Some kind of structure is present;
   b) the (unknown) sediment structure leads to a broad reduction in the reflection coefficient with increasing frequency and angle and also adds a largely random looking pattern of reflection highlights;
   c) weakly suggest layering due to vestiges of interference patterns seen from 3–10 kHz;
   d) are partially explained by plane layering, but plane layering does not explain the randomness.

2) Swale Site: Inspection of the reflection data at the swale site [see Fig. 6(a)] shows no critical angle (i.e., an angle below which the reflection coefficient is approximately

---

[2]The intercalating model with two identical sediments was the simplest way (following Occam's razor) to build up a layered model, i.e., using known sediment speeds for two distinct sediment types and assuming that some process, e.g., large storms, creates inter-bedding from two different sediment sources (e.g., estuarine and marine). Other different layered models could be postulated.

[3]Unpublished modeling by Todd Hefner based on sediment grain size analysis indicates that negative dispersion is not expected for frequencies below about 100 kHz in this area.

TABLE III
SWALE SITE GEOACOUSTIC PARAMETERS

Thickness (m)	Sound speed (m/s)	Attenuation (dB/m/kHz)	Density (g/cm^3)
0.65	1555	0.45	1.6
	1680	0.2	1.9

The water sound speed is 1524 m/s.

unity). This means that the sound speed must be less than $c_s \leq c_w / \cos(\theta_{\min})$, where $\theta_{\min}$ is the minimum observed angle in the measurement. This leads to $c_s \leq 1585$ m/s. The lower sound speed (relative to crest site) was not surprising given that core data taken on the ebb tide delta showed a significant fine fraction [10].

Inspection of the swale site reflection data clearly shows an interference pattern below 30°. The interference pattern is caused by classical quarter-wavelength ($k_{jz} d_j = m\pi/2$) and half-wavelength resonances ($k_{jz} d_j = m\pi$), where k_{jz} is the vertical component of the wavenumber in the jth layer, d_j is layer thickness, and m is an integer. These relations indicate a single layer and provide means to estimate layer thickness, ~0.65 m. The layer properties were informed by analysis of normal incidence reflection data (see Section IV) and are given in Table III.

The underlying half-space properties were informed by [10] which indicated that the mid-sand-sheet reflector was below the poorly sorted sediment by about 1 m or less, which conforms closely with the layer thickness, 0.65 m estimated from the wide-angle reflection data. Lacking other specific information, we assume the same properties for the mid-sand-sheet-reflector as the sand at the crest site (see Table III). The simulation result [see Fig. 9(b)] based on this geoacoustic model shows an interference pattern that is reasonably similar to the data [see Fig. 9(a)] at angles below 30°. The interference pattern at steeper angles is not apparent in the data. Fig. 9(c) and (d) will be discussed in the following section.

3) Effect of Rough Boundaries: It was hypothesized that perturbation of the interference pattern could be caused by layer roughness. This hypothesis was explored by forward modeling using the same geometry as in the at-sea experiment. The reflected field was computed in the time domain from a point source and receiver above a layered seafloor and the reflected time series data were then processed in the same manner as the measured data. The principle approximations in the model (see [15]) are the tangent-plane approximation, the Born approximation (multiple reflections between interfaces are neglected), and the flat-interface approximation for computing the transmitted field. The latter two approximations follow closely from Langston [16] and thus the model will be referred to as the Langston–Kirchhoff (L–K) model. The roughness is parameterized assuming a von Karman spectrum, $W(k) = w/(k^2 + L^{-2})^{\gamma/2}$, where k is the spatial wavenumber, w is spectral strength, γ is spectral exponent, and L is the spectral cutoff length.

The L–K model was verified first with flat interfaces by a comparison with numerical evaluation of the Sommerfeld integral (which is an exact solution of the reflected field from a point source above a plane-layered medium). It was then verified for rough interfaces using a time-domain finite-difference software package Simsonic [17] for the layered environment of Table III and a realization of roughness parameters discussed in the following paragraphs. The L–K model is capable of treating both 2-D and 3-D environments (1-D and 2-D rough surfaces) and a few 3-D simulations were performed. The 3-D computations were 400 times slower than 2-D for the frequency range and spatial domain of the simulation problem here. Since the general trends and features of the 3-D and 2-D models were similar for this environment and geometry, the 2-D model was used most extensively and those results are presented here. The L–K model also treats in-plane and out-of plane dipping layers, but for the simulations here, the mean interfaces were assumed to be parallel to the sea surface.

The goal of the simulations was to determine if general features of the interference perturbations in the data at both swale and crest sites could be explained by interface roughness. As far as was practical, environmental parameters were drawn from measurements at each site.

a) Swale Site: The geoacoustic properties at the swale site (see Table III) were inferred by modeling. 1-d roughness statistical parameters, Table IV, were estimated by Hefner [18] from laser line scanner from the water sediment interface. Though the laser line scanner data were collected on a ridge, not a swale, these were assumed to be pertinent to both environments. Since no estimates of the spectral cutoff were available, five realizations were drawn for various values of spectral cutoff length, L. Each realization consists in applying the von Karman spectrum with the different cutoff length on an identical white random spectrum (but different between the water-sediment interface and the base of the layer). The Gaussian distributed interface slopes for these parameters have a standard deviation of 3° at $L = 0.03$ m and 9° at the maximum spectral cutoff value, $L = 1.8$ m.

No roughness measurements were available for the lower layer boundary and as a first approximation, the roughness statistics were assumed to be identical at both interfaces. The simulation results are shown in Fig. 10. Note that high reflectivity values near 10 kHz at 15°–25° are numerical artifacts.

Before discussing the simulations, it is helpful to consider effects of the Fresnel zone, or the size of the insonified region on the rough surface (see Fig. 11). The smallest in-plane Fresnel radius is about 1 m, which occurs at the highest angle and frequency. The largest in-plane Fresnel radius is about 10 m which occurs at the lowest angle and frequency. The Fresnel radius is an important spatial scale that significantly affects how the roughness influences reflection. Returning to the reflection simulation with rough boundaries (see Fig. 10), the results in the first row, $L = 0.03$ m, indicate that roughness has practically no effect on the reflection coefficient at all angles and frequencies. This can be understood by comparing $2\pi L$ with the Fresnel radius, ξ. When the Fresnel zone is much larger than the cutoff scale, ($\xi \gg 2\pi L$), the acoustic field at the receiver is averaged across many roughness scales, and the roughness has little net effect on the reflection coefficient.

When $2\pi L$ is on the order of and larger than the Fresnel zone and there is sufficient power in the low wavenumber part of the
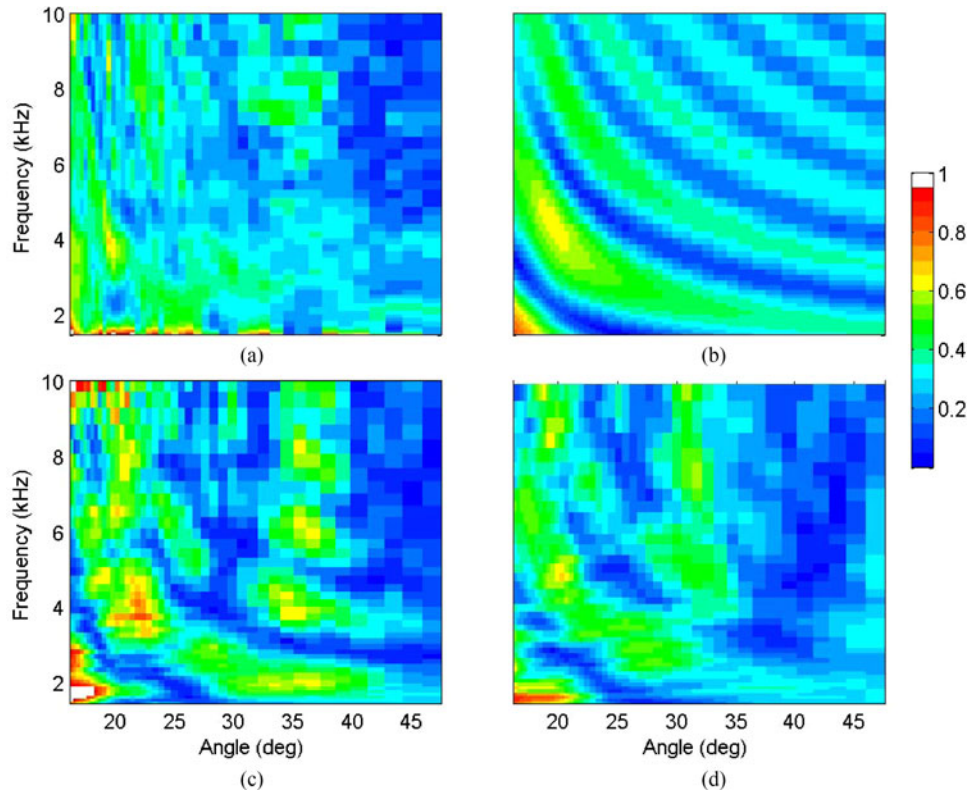
Fig. 9. Swale site seabed reflection (a) data and (b)–(d) simulations. (b) single plane layer over a half-space (see Table III), which roughly captures the measured data below 30°, (c) Table III with roughness parameters of $L = 0.6$ m $\gamma_1 = 3.43$ $w_1 = 0.0039\,m^4$ for the top and bottom of the layer and (d) same as (b) with $L = 0.3$ m and modified basement parameters of 1640 m/s and 1.65 g/cm³.

TABLE IV
ROUGHNESS PARAMETERS USED IN THE SIMULATIONS

Data Source	1-D spectral strength $\boldsymbol{w}_1\ (m^4)$	1-D spectral exponent γ_1
Laser line scanner [18]	3.9×10^{-3}	3.43
Fit to multibeam and laser line data (Appendix 2)	2.12×10^{-5}	1.85

heterogeneity spectrum, the roughness plays a more significant role and the interference pattern is perturbed. This can be seen in row 2, $L = 0.2$ m (Fig. 10), for the high angles and high frequencies (above ∼5 kHz), where the interference pattern is perturbed. Note that at low angles and frequencies, however, the interference pattern is not perturbed much, since in that region $\xi \gg 2\pi L$.

It is useful at this point to refer back to measured data, Fig. 9(a). The fact that the interference pattern is most clearly visible at low angles can now be understood in light of Fresnel zone effects. Note also that the Fresnel zone (see Fig. 11) is a relatively weak function of frequency at the low angles, say below 30°; the data show this same trend. That is, the interference pattern is most clearly seen in the data below 30° and at all frequencies with some minor perturbation at higher frequencies.

As the spectral cutoff increases further, e.g., $L = 0.6$ m in row 3, Fig. 10, more of the frequency-angle domain is affected by the roughness and broad patterns emerge. For example, in

row 3 realization 1, there are reflection peaks at 30°, 40°, 50°, 80° that can be seen across a range of frequencies. The broadband nature can be explained by focusing from seabed curvature (from either layer interface). Theory predicts that the reflection amplitude due to focusing increases with increasing frequency. For example, above a concave hemispherical boundary, the focused field amplitude (i.e., reflection) at a distance equal to the radius increases linearly with frequency (e.g., [19]). This amplitude increase is simply a manifestation of conservation of energy, where the size of the "focal spot" decreases with increasing frequency. One example of this can be seen in row 5 realization 2 at about 55°, where the high reflection coefficient due to focusing increases in amplitude and narrows in angular range with increasing frequency (due to the diminishing in size of the focal spot). The oscillatory behavior of the frequency dependence in this (and other examples in Fig. 10) are caused by the interaction of the focusing with the layer interference pattern.

Adjacent to the broadband focusing highlights, there are broadband nulls. These are caused by defocusing (convex regions of the seafloor within the Fresnel zone). For each roughness realization, the focusing/defocusing regions move to different locations in angle space (as expected). A key point here is that interface curvature can perturb (or even destroy) the interference pattern. The defocusing effects also appear in the measured data. Note that the broadband reflection highlight at about 35°, Fig. 9(a), may be from focusing and the reflection nulls on either side due to defocusing. The data are
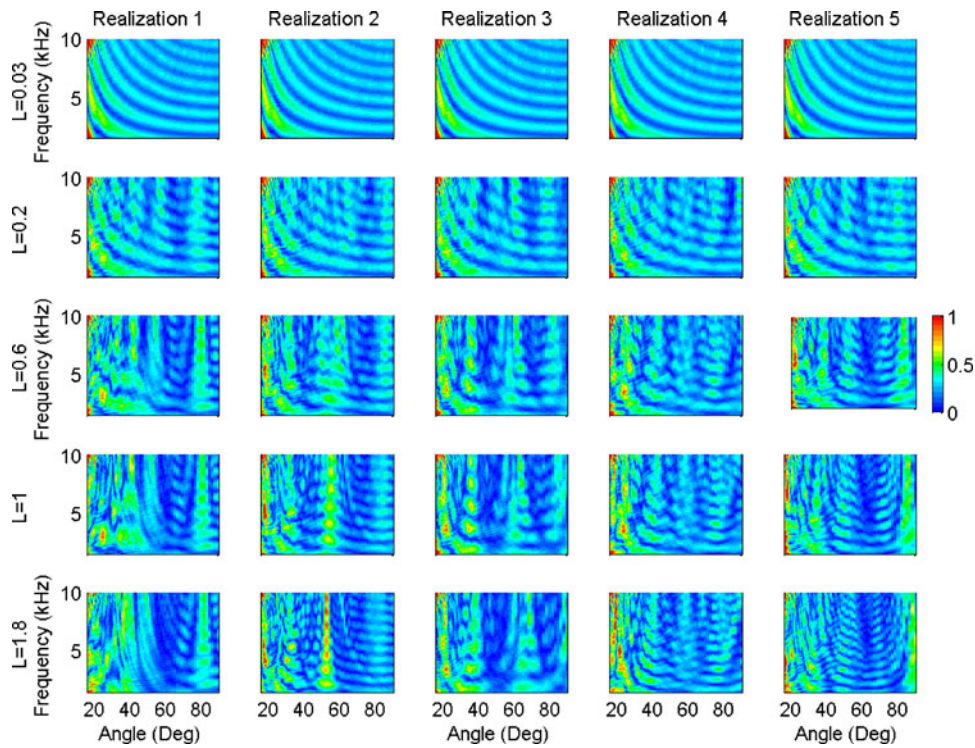
Fig. 10. Simulation of experiment data, i.e., using the same experiment geometry, with estimated roughness values from laser line scanner data, Table IV, for various realizations (columns) and values of spectral cut-off, L (rows). Geoacoustic properties are given in Table III.
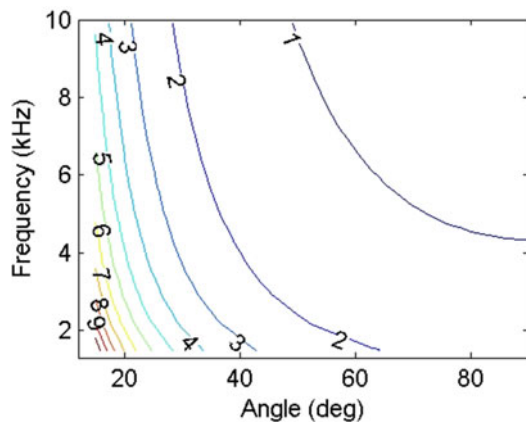

Fig. 11. In-plane Fresnel zone radius for the experimental geometry employed in the reflection measurements.

compared with simulation in Fig. 9(c) ($L = 0.6$ m, realization 3 in Fig. 10). Note that the simulation and observations show a number of similar features as follows:

1) the existence of a broadband reflection highlight at 35°;
2) the highlight oscillates in frequency;
3) there are reflection nulls on either side of the highlight; and
4) the null is less "deep" at shallow angles (25°–32°) than at steeper angles (40°–48°).

The simulation in Fig. 9(c) clearly has stronger perturbations than observed in the data; the simulation result for the same realization with $L = 0.2$ m show weaker perturbations (see

$L = 0.2$ m, realization 3 in Fig. 10). A spectral cutoff length $0.2 < L < 0.6$ m was expected to give a closer match to the data, which is the case seen in Fig. 9(d) with $L = 0.3$ m. In Fig. 9(d) results, the basement sound speed and density were reduced (see caption) to mimic a positive density and sound speed gradient in the upper layer. The primary effect of the gradient with respect to the reflection coefficient for this problem is to lower the impedance contrast at the basement. Reducing the basement sound speed and density is commensurate and computationally simpler. The net result of the gradient, or reduction in basement impedance contrast, is to reduce the peak-to-null amplitudes in the interference pattern. The simulation in Fig. 9(d) captures much of the structure in the measured data. Though it appears that in the measured data, the impedance contrast between the two layers was even lower than modeled, further tuning of the geoacoustic or roughness parameters was not attempted.

The simulation is instructive on one other point, i.e., the reflection coefficient is only weakly sensitive to L values much greater than the Fresnel zone. This can be seen in Fig. 10 by examining the similarity of the reflection coefficient for a given realization when $L \geq 0.6$. From an information content point of view, this means that the presence of perturbed interference patterns in measured data can inform a lower bound to L, but cannot inform an upper bound if the data space is such that $\xi \ll 2\pi L$.

In addition to the roughness parameters from the laser line scanner (spatial resolution 4 mm), it was desirable to estimate roughness parameters from multibeam bathymetry data [20] (spatial resolution 1 m). This was of interest since the spatial

wavenumbers that control reflection are smaller than those estimated by the laser line scanner. The 1-D spectral parameters estimated from the bathymetry data, are quite different (details are given in Appendix II). The roughness parameters used in simulations (see Table IV) were derived by a fit across the multibeam and laser line data, ignoring the low wavenumber part of the laser line data.

The reflection coefficient simulation with these parameters showed a weak perturbation of the interference pattern for all values of L. Even at large values of L, the perturbations to the interference pattern were much weaker than those in the data. This is so because for a relatively low spectral exponent, the small-scale roughness (high wavenumbers) imposed on the large-scale curvature (low wavenumbers) prevent high coherence required for significant focusing. When the spectral exponent is relatively high, the power in the large-scale roughness/curvature is large compared to the small-scale roughness so that strong focusing can occur (as in Fig. 10). Thus, two conditions are needed for focusing, a relatively high spectral exponent and $2\pi L\sim > \xi$.

It was clear that the multibeam bathymetry-derived roughness parameters at the top and bottom of the layer could not explain the observations. This left the possibility that a subbottom interface with higher roughness at low wavenumbers could explain the data. This seems plausible since the lower layer is coarser grained in nature, and could have formed in a higher energy environment (e.g., lower sea level) than the upper layer. This possibility was explored using the bathymetry-derived spectral parameters at the water sediment interface with $L_{top} = [0.15, 1, 3, 5, 9]$ m, and the laser line scanner parameters on the lower layer with $L_{bottom} = [0.03, 0.2, 0.6, 1, 1.8]$ m. Note that the spectral cutoff value of L is five times smaller at the bottom of the layer than at the top; this was done because using the L_{top} values for the bottom layer would lead to unreasonable values of rms roughness in the bottom layer.

The reflection simulation results using a higher roughness at the lower layer showed generally weaker perturbations than Fig. 10 (as expected) and most of the 25 results (5 realizations times 5 values of L) showed weaker interference perturbations than the data. One realization showed strong perturbations, but this was due to a peak in the bottom layer height. The peak led to a very thin layer thickness (0.2 m) at $\sim$30° and a highly perturbed interference pattern, but quite dissimilar to the data. The case of equal (laser line scanner) roughness statistics at both interfaces (see Fig. 10) exhibited features more similar to the data than did this simulation.

b) Crest Site: Returning now to the crest site, interface roughness effects were explored also using the L–K model. Before discussing the roughness simulations, the L–K model was tested with a flat interface [see Fig. 8(e)] and comparing it with the exact solution [see Fig. 8(a)]. Note that the L–K model captures the relevant physics quite well both at and below the critical angle. This gave some confidence in applying the model to the crest site. Roughness effects were simulated using the laser line scanner roughness parameters (see Table IV) with $L = 0.03, 0.2, 0.6, 1.8$ m for five different roughness realizations. The result that was most similar to the crest site data is shown in Fig. 8(f), where the high levels from 9–10 kHz and

15°–25° are numerical artifacts. Note several broadband features from focusing/defocusing. Though a few similar features are seen in the observations [see Fig. 8(d)], the similarities are not compelling and the differences are significant. The agreement below the critical angle is rather poor and roughness does not explain the reduction in the reflection coefficient at high frequencies and high angles. The other simulations $L \geq 0.2$ m had much stronger focusing/defocusing effects than observed in the data.

Simulations were also performed at the crest site for roughness in the layered case. Again, the L–K model with flat layer interfaces [see Fig. 8(h)] was compared with the exact solution [see Fig. 8(g)]. The model performs well above the critical angle, but poorly below the critical angle due to the neglect of multiple interactions within a layer, and the presence of thin layers in the geoacoustic parameters (see Table II). Both roughness parameter sets from Table IV were employed to model roughness at all and combinations of several layers. For many of the realizations, there were strong focusing/ defocusing effects not observed in the data. The realization shown, Fig. 8(h), approximately captures the higher levels at about 60° across a wide frequency band seen in the data, Fig. 8(d). However, the simulation still has a more organized frequency-angle behavior than does the data.

In summary of the crest site simulations, interface roughness added to the half-space and layered cases led to some (modest) changes in predicting trends observed in the data. The angular and frequency dependence with roughness do not closely mimic the observations. Another possibility for explaining the observations is sediment volume heterogeneities. This was not explored.

IV. NORMAL INCIDENCE REFLECTION

The wide-angle reflection analysis considered two locations —a ridge and a swale separated by $\sim$6 km (see Fig. 2). The motivation for the normal incidence measurements was to understand the lateral variability of the water-sediment interface at smaller scales, from O(1) m to O(100) m.

The normal incidence reflection coefficient was measured using a reference hydrophone approximately 2 m above the source on the same tow cable and was collected at the same time as the wide-angle measurements. Reference phone problems rendered data viable only along one 440-m track (May 9, 2013) but fortuitously this was close to the swale site wide-angle reflection track, see Fig. 12(a). Due to the tight geometry constraints on the source depth and maximum depth of the source tow cable required by the wide-angle data, the sea surface reflected path on the reference hydrophone arrived before the bottom reflected path by only $\sim$1.6 ms. On the track with viable data, the sea surface was sufficiently rough so that the scattered coda from the sea surface path obscured the arrivals following the bottom reflection, but did not bias the bottom reflection peak. Thus, instead of being able to use the bottom reflected time series and form a frequency domain reflection coefficient, the magnitude of the peak broadband (1.4–12 kHz) bottom reflection coefficient was used to make inferences of the sediment properties near the water-sediment interface ($\sim$upper 0.15 m).
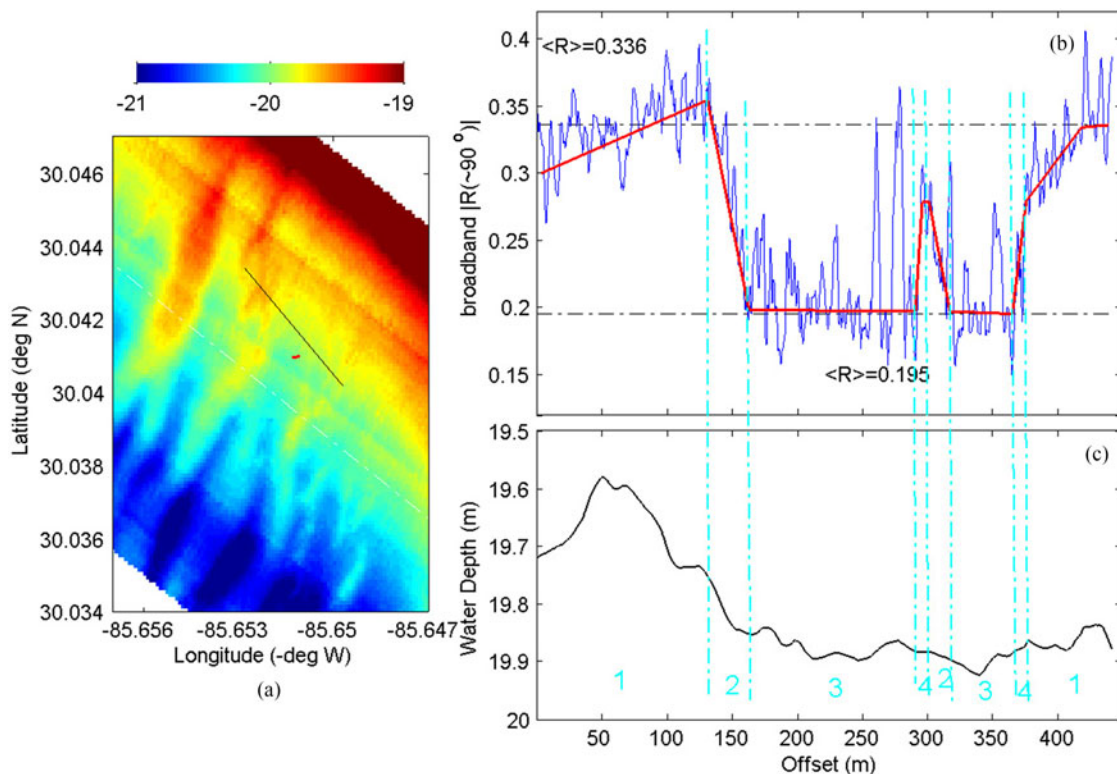
Fig. 12.   (a) Bathymetry (meters) with normal incidence reflection track (black line) from northwest to southeast. The swale site wide-angle reflection track is shown in red trending west-southwest (the line indicates only the bottom interacting portion of the track); (b) Normal incidence reflection coefficient data (blue) along with interpreted "reflection regimes" (cyan dotted lines and numbers) and a simplified fit (red) to the data. (c) Along-track 10 m resolution bathymetry data from [20].

The reflection coefficient was computed by taking the ratio on every ping of the bottom reflected path peak and the direct path peak, correcting each for spherical spreading. Source amplitude variations were negligible, but were accounted for. The transit speed was about 1.5 m/s, and the pulse repetition rate 0.5 s, so the pulse-to-pulse offset in the specular point on the seabed is 0.75 m. Thus there is significant overlap in the Fresnel zone on consecutive pings: 72%, 53%, 32% at the lower, center, and upper end of the band, respectively (see the Fresnel zone radii in Fig. 11 at 90°).

A. Seabed Lateral Variability at the 1–10-m Scale

The reflection results were averaged over three pings (a lateral extent on the seabed of 3.5 m at the center of the band) and are shown in Fig. 12(b) (blue line). Note the substantial drop in reflectivity at ∼150 m, where the change is almost a factor of 2 in amplitude. Both system (e.g., source depth or amplitude variation) and environmental factors to explain this drop were explored. However, the observed variations are not due to system effects; both the source and receiver were essentially omnidirectional, so motion from towing would have negligible impact and the source–receiver positions were carefully measured on each ping. The variability in the reflection coefficient must be due to seabed effects.

There are two other large changes (a factor of ∼2) in reflection amplitude: at 260 and 275 m. These were examined on an

individual ping basis and it was found that each peak occurs from a single ping. Since the neighboring pings exhibit significantly lower amplitude but significant Fresnel zone overlap, the only reasonable explanation is focusing from bathymetric curvature. The increased reflectivity at 300 m by contrast occurs over many consecutive pings.

There is a spatial periodicity clearly observed in the reflection data [see blue curve in Fig. 12(b)], which was estimated from normalized data using a split window normalizer (averaging window of 9.5 m and a guard band of 12.75 m). The main peak of the spatial periodicity is at 26 m with a secondary peak at 43 m. These periodicities do not correspond with any motion of the source or receiver, thus they are not artifacts related to system effects. It is possible that there are small-scale bedforms unresolved in the bathymetry leading to either slight focusing and defocusing or that other geological processes lead to fluctuations on those scales.

B. Seabed Lateral Variability at the 10–100-m Scale

A comparison between reflectivity and bathymetry is shown in Fig. 12(b) and (c). It should be noted first that the reflection data positions may be biased forward along the track by some meters because the source and receiver trailed slightly behind the GPS receiver fixed on the back of the catamaran. Given the measured length of cable between source and catamaran (13.4 m) and the estimated source depth, ∼10 m, the maximum

GPS-to-source horizontal offset, i.e., for a straight line cable, is ∼9 m. The expected catenary cable geometry would reduce that offset. Currents may have deflected the source from the plane of the tow direction, but cross-track deflections would be much, much less than 9 m. In summary, the track position may be biased up to 9 m along track and a few meters cross-track. Positional errors on the extracted multibeam data are less than 1 m.

One salient point is the lack of obvious correlation between the reflection coefficient and the bathymetry. The sand ridge crest peak (at 46 m) is separated by more than 80 m from the peak of the reflection coefficient (130 m). Also, near the end of the track, there is a sharp rise in the reflection coefficient, but the bathymetry is nearly flat. Only the central and lowest part of the track has a reasonable correlation with the lowest reflection coefficient values. It is important to observe that the bathymetry varies only 30 cm along the track; the water depth changes are very small.

The reflection data suggest four regimes, which are delineated in Fig. 12(b) and (c) in the vertical dotted cyan lines and numbered 1 to 4. First, the major features are described, i.e., neglecting the small feature at about 300-m offset. Regime 1 seems related to the sand ridge crest, but oddly, the reflection coefficient steadily increases from the lee side to almost precisely halfway down stoss side (from ridge peak to trough). The current direction is from the Southeast. At this point, there is a rapid drop in reflectivity and this zone is called Regime 2. Regime 3 has generally low reflectivity values (with many peaks) and corresponds with the deepest part of the bathymetry. At about 375 m, the reflectivity rises sharply (Regime 4), even faster than the decline in Regime 2. The final portion of the track looks similar in reflectivity values to Regime 1, though with a steeper slope.

Returning now to the 23-m-long feature at 300 m, note that this occurs on the stoss side of a very small ridge or mound in the swale (the mound is about 85 m in length, ∼250–335 m offset, and only 5 cm high). The rapid rise in the reflection coefficient at ∼300 m has a similar slope with that at 375 m and thus is designated as Regime 4. This regime is followed by a decrease in the reflection coefficient very similar to Regime 2. In fact, the Regime 2 slope, $dR/dx = -0.005$ m^{-1}, where R is the reflection coefficient and x is offset distance, is essentially identical at 150 and 310 m. The slope in Regime 4 is about twice as large and with the opposite sign, $dR/dx = 0.0123$ m^{-1} at 300 m and 0.0096 m^{-1} at 375 m.

In an effort to quantify the geoacoustic variability along this track, the density and sound speed were first estimated at the average value of the simplest regimes 1 and 3 (shown in black dash-dotted line). It is well known that there are numerous difficulties (i.e., ambiguities) in estimating density and sound speed from normal incidence reflection data. Reflection amplitudes are influenced by many mechanisms including roughness, sediment volume scattering, seafloor curvature, layering, gradients, and impedance changes. Resolving contribution from individual mechanisms is generally not possible and for simplicity, here, all mechanisms are ignored except the latter, i.e., the seafloor is assumed to be a perfectly flat homogeneous half-space for each consecutive ping. Ignoring the roughness can be justified by

noting the reflection coefficients are averaged in space, across many roughness scales and thus should average out to the flat case. With these assumptions, it is possible to estimate the along-track sediment impedance Z (product of density and sound speed)

$$Z = Z_o \left(1 + R(\pi/2)\right) \left(1 - R(\pi/2)\right)^{-1} \quad (1)$$

where Z_o is the seawater impedance. From the sediment impedance Z, the sediment sound speed and density are estimated from the empirical relations of Bachman [13]. These assumptions applied to Regime 1 ($R = 0.336$) result in a sound speed of 1684 m/s and density of 1.87 g/cm^3, which compare closely with the estimated sound speed (from the critical angle) of 1680 m/s from the wide-angle data at a ridge crest along the clutter track. The two crests are about 6 km apart, but the congruence of the sound speed suggests ridge crest geoacoustic properties may be similar in this region. In the swale, Regime 2 ($R = 0.195$) yields a sound speed of 1544 m/s and a density of 1.68 g/cm^3. This is in concordance with the nearby swale site wide-angle measurements, which indicated that the sound speed must be less than about 1585 m/s.

The fact that the approximate and average results in regimes 1 and 2 do not appear to be in gross error, suggested that including all the regimes would not be unreasonable. In this analysis, smoothing was performed such that only relatively large-scale fluctuations with a high probability of being related to geoacoustic variability were preserved. The smoothed reflection data for this part of the analysis is shown in Fig. 12(b) in the red line.

The result of applying the flat homogeneous assumptions and the empirical equations to the spatially smoothed reflection data is shown in Fig. 13. Note that there is a substantial variation in both density and sound speed across the short track. This is somewhat surprising given that the swale and crest differ in water depth only by 0.3 m. It is not understood at this time why the geoacoustic properties (impedance) increase from the ridge lee side to the crest and then continue increasing until halfway down the stoss side.

The lower sound speed and density in the swale (Regime 3) clearly indicates a higher concentration of clay and silt particles than on the ridge. In the swale, there is a significant (ostensible) change in impedance at 300 m which likely represents a band of coarser grained sediment. The width of the band is about 23 m, which is comparable to the secondary peak in the spatial periodicity (at 43 m for a full cycle, 21.5 m for a half cycle or band).

It is of interest to examine any correlations between the normal incidence reflection data and 400-kHz backscatter; see Fig. 14. It is difficult to see any clear correlation. There are two or three higher backscatter (lighter color) lines perpendicular to the track in the first one-third of the track (from Northwest to Southeast). At other locations in the survey, the high backscatter occurred on the lee side of ridges, though it is not clear here if these features are related bathymetry [see the first 135 m; Fig. 12(c)]. In general, there does not appear to be strong correlations between the 400-kHz backscatter and the 1.5–10-kHz reflection data, except to note that the third lineal feature is roughly the end of Regime 1 (which may be coincidental) and
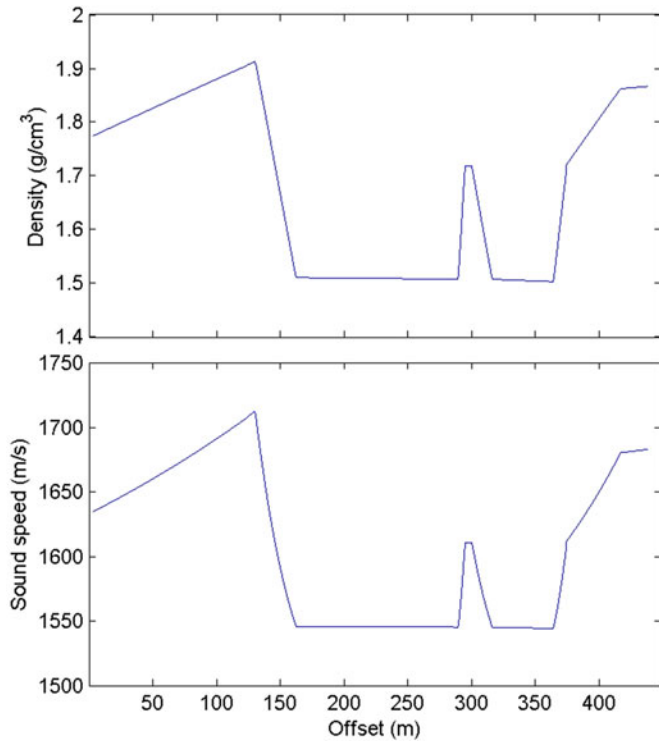
Fig. 13. Estimated density and sound speed from smoothed normal incidence reflection data along a track [see red line in Fig. 12(b)] from Northwest to Southeast near the TREX13 main reverberation line.

Fig. 14. Multibeam backscatter data [20] with normal incidence track (white line trending from Northwest to Southeast, ∼440 m in length) and wide-angle track (short East-west white line, ∼25 m in length). The gray scale spans 23 dB with 0 dB in black and 23 dB in white.

the lineal features are separated by about 40 m, which was a scale apparent in the reflection data. One potential correlation is that the band of high reflection (likely coarser sediment) at 300 m [Fig. 12(b)] is near the slightly lower (darker) backscatter, at about 2/3 of the distance along the track (from Northwest to Southeast).

The backscatter data do not show any strong variations along the wide-angle reflection track (short white line trending East–West). There is, however, a thin lower backscatter (darker) arc which intersects the track near its center. It is not clear what the implications of this are. Also note that the otherwise apparent uniformity of the backscatter for the rest of the short track should not necessarily suggest surficial sediment homogeneity (given the lack of correlation of the high frequency backscattering with the normal incidence reflection track).

V. SUMMARY AND CONCLUSION

Measured wide-angle and normal incidence seabed reflection coefficients off the coast of Panama City, FL, USA, contain valuable information on the geoacoustic properties. However, the most potentially informative (wide-angle) observations at two sites also raised a puzzling question. Neither dataset showed the usual (in our experience) interference pattern caused by classical one-half and one-quarter wavelength resonances that occur in plane-layered media. Though there is evidence for layering at the swale site and the crest site, a mechanism (or mechanisms) exists that perturbs the interference patterns. Since the
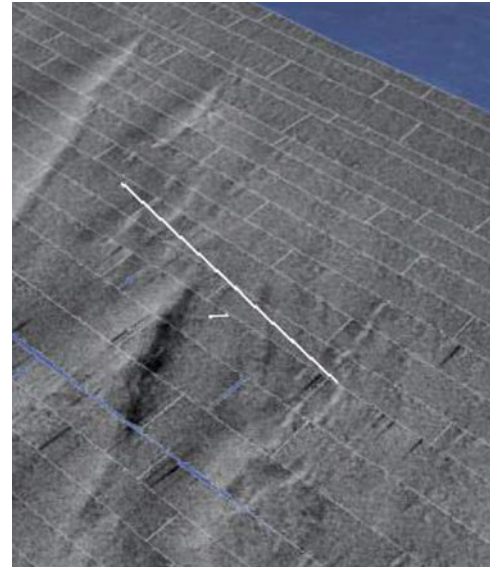
interference patterns require flat parallel boundaries, boundary roughness is one hypothesis for the perturbations. A second possibility is the presence of strong volume heterogeneities which would lead to decorrelation of the up and down-going wave fields in a layer.

Only the roughness hypothesis was examined. Simulations performed at the swale site explored the effects of roughness on the wide-angle interference patterns. The simulations showed similarities with measured data when 1) the spectral exponent was large, i.e., much greater power in the low spatial wavenumber spectrum relative to that in the high wavenumbers; and 2) the Fresnel zone was of the order or smaller than $2\pi L$, where L is the spectral cutoff. The main mechanism was focusing and defocusing of the acoustic field due to interface curvature, which results in broadband peaks and valleys superposed on the interference pattern and in some cases destroying the interference pattern entirely.

The broadband peaks/nulls in the swale site data appear to be due to focusing/defocusing. The roughness hypothesis appears to be correct at this site inasmuch as simulations showed features similar to the measured data. Furthermore, an alternative hypothesis of scattering from volume heterogeneities would not produce focusing and defocusing. Though the evidence is strong, the roughness hypothesis cannot be completely verified inasmuch as layer roughness statistics are insufficiently known. The lower layer roughness statistics are not known at all (and very difficult to obtain), and the water-interface statistics are incomplete (lacking an estimate of spectral cutoff) and uncertain. Two estimates of the roughness statistics were considered: one derived from laser line scanner data which indicated focusing comparable to the data when the spectral length was employed as a free parameter. The roughness statistics derived from multibeam bathymetry data did not show comparable focusing for any reasonable value of spectral cutoff length. In summary, simula-

tions indicate interface roughness is the likely explanation for the swale data interference perturbations.

Normal incidence reflection data were employed to estimate surficial sediment sound speed and density along a track extending from one ridge to the swale and partially onto another ridge. The track was located ~3.5 km Southeast from the TREX13 moored reverberation source and receiver, where poorly sorted sediments associated with the ebb tide delta dominate the surficial sediment fabric. The elevation change between ridge and swale there is rather small, about 0.3 m. The normal incidence data showed clear signs of focusing effects, adding additional credence to the roughness hypothesis as an explanation for the nearby swale site measurements.

In summary, the sediment geoacoustic observations from the wide-angle and normal incidence reflection measurements indicate the following.

1) The wide-angle reflection data at the crest site show the following.
   a) The data cannot be modeled with the assumption of a homogeneous half-space. The half-space assumption does not correctly model the angle or frequency dependence of the data below the critical angle, at the critical angle or above the critical angle.
   b) The data can be modeled reasonably well with the assumption of layering. The layered assumption leads to general correspondence with the data below the critical angle, at the critical and (largely) above the critical angle. It does not capture seemingly random perturbations at some angles above the critical angle. These perturbations might be explained by the addition of layer roughnesses, but more likely by the addition of volume scattering within the layer. Sound speed, density, and attenuation gradients also seem to be important in explaining the data.
   c) The data indicate that the sound speed was nearly independent of frequency, 1.5–10 kHz, due to the behavior of the critical angle.
   d) The data yield a sound speed and density similar to that at a ridge close to the swale site 6 km to the east.
2) The wide-angle data at the swale site can be modeled with a single layer with roughness at both boundaries. Since there is a low-angle interference pattern, the data cannot be modeled by the half-space assumption. The roughness parameters that reasonably explain the data were derived from laser-line scanner data measured at the water-sediment interface and applied also at the subbottom layer interface with spectral cutoff treated as an unknown (free) parameter. A spectral cutoff value of $L = 0.3$ m yields simulated results comparable to the measured data.
3) Normal incidence reflection along a 440-m-long track near the swale site indicates the following.
   a) The clear presence of focusing/defocusing, which strengthens the focusing/defocusing interpretation at the nearby swale site.

   b) Four distinct geoacoustic regimes from one ridge crest to another that appear loosely correlated with bathymetry: lee to stoss side of ridge crest, halfway down the stoss side to the base of the swale, the swale, and the transition between the swale and the lee side of the next ridge crest [see Figs. 12(b) and 13]. In the swale regime, there is a small mound, 5 cm in height that exhibits regimes that are similar to those on the larger ridges.
   c) Substantial geoacoustic lateral variability. For example, the sound speed changes from 1550 to 1700 m/s in a lateral distance of 20 m on the stoss side of the ridge. The change appears to be related to water depth and position on the ridge, but water depth differences that separate the two sound speeds are only about 0.1 m [see Figs. 12(b) and 13].
   d) Spatial periodicities of 26 and 43 m, suggesting a spatial periodicity in the sediment structure in the swale.

The underlying cause of the geoacoustic variations, e.g., the geologic and/or hydrodynamic mechanisms that control the geoacoustic spatial variability are not understood at present.

The analysis did not employ the planned plane-layered inversion methods. Nevertheless, the sediment properties presented here, though somewhat crudely estimated from theory and forward modeling, may have some value for future scattering, propagation, and reverberation studies.

APPENDIX I

A. Geometry Reconstruction

Neither the time nor position was measured with sufficient accuracy at the source and receiver to determine the precise time of signal transmissions. Thus, instead of having absolute travel times, relative travel times between direct and bottom reflected, and direct and sea surface reflected arrivals were employed to estimate source–receiver offset and other parameters of interest. A ray-based forward model [21] was applied in a Bayesian inversion framework to estimate the source–receiver offsets (ranges), reflection angles at the seabed, source depth, and water depth together with rigorous uncertainties for all parameters.

Fig. 15 shows a representative result for the measured relative travel time data (blue) and the fits (red) for two receiver depths. The first 120 data points are the direct-bottom relative travel times for the upper receiver. The second 120 data points are the direct-surface relative travel time data and fits for the upper receiver. The variation in measured travel time fits from sea surface swell is apparent (blue line from 120–240) compared to the smooth (assumed flat surface) of the model. The remaining 240 data points pertain to the lower receiver.

The uncertainties associated with the four parameters of interest are shown in Fig. 16. The minimum source–receiver offset (range) for this leg was about 4 ± 0.1 m, with an uncertainty that increases with increasing range. The resulting uncertainties in the seabed angle estimation are shown in the top plot, and are about 1° or less.
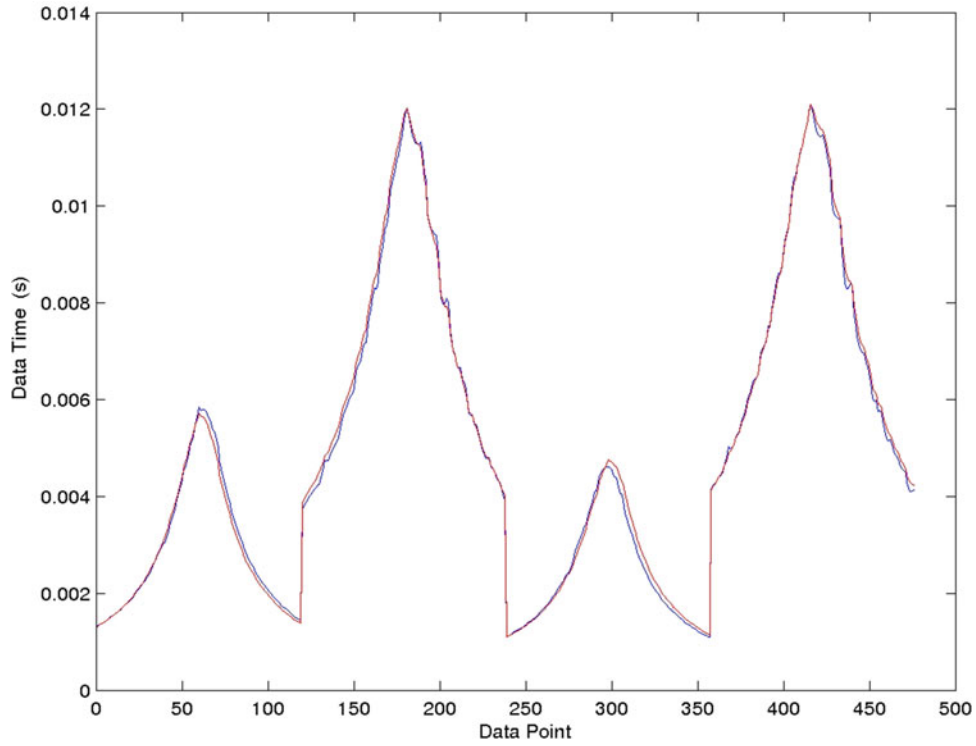
Fig. 15.   Relative travel times for the direct-bottom and direct-sea surface paths for the measured data (blue) and the fits (red) using a ray-based inversion.
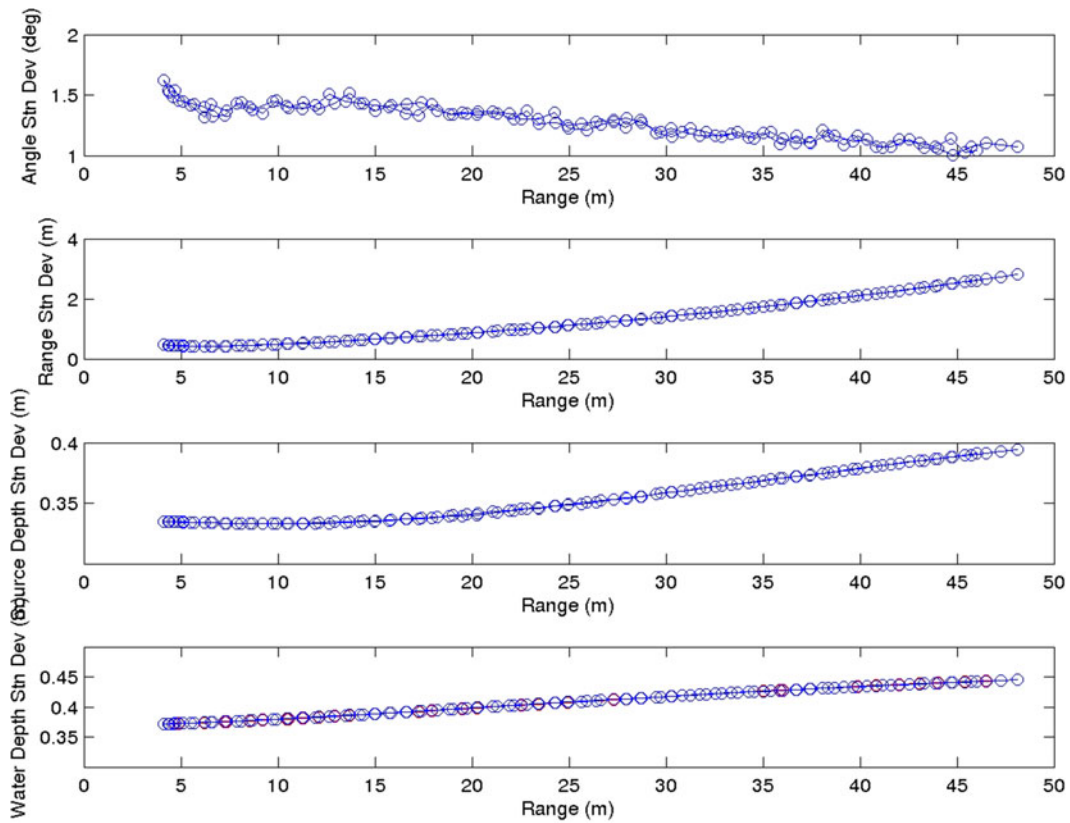

Fig. 16.   Uncertainty estimates for the parameters of interest from the ray-based relative travel-time inversions (data fits shown in Fig. 15).
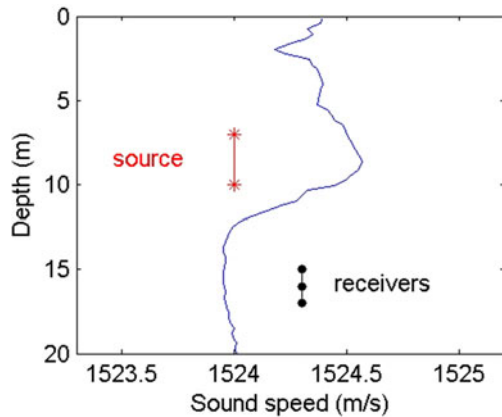
Fig. 17. Sound speed profile on May 5 with the range of source and receiver depths indicated.

The sound speed profiles were nearly isospeed (an example is shown in Fig. 17), though refraction was not negligible in estimating the experiment geometry. Refraction effects were included in the ray-based Bayesian estimation. The Bayesian estimates of the source–receiver geometry were compared with independent measurements by computing source tow speed, v

$$v = \frac{|r_j - r_{j-1}|}{\eta \cos \theta} \tag{2}$$

where r_j are the estimated source–receiver offset ranges, η is the pulse repetition rate (in seconds), and θ is the angle in the horizontal between the tow radial and the receiver

$$\sin \theta = \frac{\min |r_j|}{r_j}. \tag{3}$$

The ray-based travel-time Bayesian inversion tow speed estimates were compared with those from a catamaran-mounted GPS, and from relative-velocity estimation using the Doppler cross-power spectral phase [12] as well as the traditional ambiguity function approach, see Fig. 18. The latter three methods are sampled at the pulse repetition rate, 0.5 s, whereas the GPS data are sampled at 5 s. The source–receiver depth difference estimated from the ray-based inversion results was used to convert relative velocities to tow speed.

The instantaneous source tow speed is a function of the ship speed (slowly varying) and the dynamics of the coupled catamaran-suspended source system moving over passing waves. Visual observations showed that the catamaran sped up when advancing down a front of a wave crest, then slowed near the trough. These fluctuations in the speed are not captured in the slowly sampled GPS data, but are captured in the other three methods, see Fig. 18. While the non-GPS methods give similar results, some differences/errors are evidence. The Doppler formula appears to underestimate the speed for transmissions 4 and 5 and perhaps 113 and 116. The ambiguity function method greatly overestimates the speed for transmission 8–13, 17, and 31. The relative travel-time inversion (Bayesian) appears robust at far ranges (small and large transmission numbers), but has two errors near CPA, which is at transmission 62. In sum-mary, all three methods follow the GPS data reasonably well. The ray-based travel-time inversion (Bayesian) results indicate the methodology for estimating source and receiver depths and range is robust except near CPA.

APPENDIX II

A. Seabed Interface Roughness Power Spectrum Estimate

Roughness power spectra were estimated using multibeam bathymetry collected by de Moustier and Kraft [20], and laser line scanner measurements collected by Hefner *et al.* [19]. In both cases, roughness measurements exist as 2-D digital elevation maps (DEMs). 1-D marginal roughness power spectra are obtained by removing a linear trend in a particular direction, applying a Hann window, performing a fast Fourier transform, and incoherently averaging in the orthogonal direction. Power spectra are normalized such that the windowing processes preserves the root mean square roughness of the original measurement.

The multibeam bathymetry estimates have a spatial resolution of 1 m × 1 m and are known to have minor residual noise from tides. Data used to estimate power spectra were confined to a square with a side length of 750 m centered at the swale site. The square was oriented such that its sides were either perpendicular or parallel to the ridge-swale crests. Marginal spectra were obtained by taking Fourier transforms both along and across the crest principle directions. Laser line scan measurements were taken near the swale site and have spatial resolution of 1 mm × 1 mm. The laser scanner was not outfitted with a compass, so the precise direction of the power spectrum estimates is unknown. Laser scanner spectra are also averaged over independent locations, as 2-D DEMs were measured at multiple locations near the swale site.

Results for marginal spectra are displayed in Fig. 19 as a function of spatial wavenumber in rad/m. Spectra are shown from multibeam bathymetry across and along the crest directions, which cover the low-wavenumber regime, as well as the spectra from the line scan measurements, which cover the high-wavenumber regime. For the multibeam spectra, attention is restricted to the wavenumber region above $2\pi/10$ m, which is approximately the scale corresponding to the largest Fresnel zone in the reflection measurements. The highest wavenumber portion of multibeam roughness spectra is not shown because it is subject to processing artifacts. For the spectrum derived from the laser scanner, attention is restricted to wavenumbers below 1100 rad/m. Above this wavenumber, the spectrum appears to be contaminated by noise.

A model power spectrum of the form $W(K) = w_1/K^{\gamma_1}$ was fit to the measured data, where K is the wavenumber magnitude, w_1 is the spectral strength, and γ_1 is the spectral slope. Model parameters were fit to multibeam and line scanner data independently, and by using both spectra together. Parameters were estimated using linear least-squares in log-log space, and can be found in Table V. The model fits are displayed as dashed and dotted lines in Fig. 19. Visually, fits to the multibeam and laser scanner spectra are quite consistent with one another and appear to form a continuous power-law spanning over three orders of magnitude. Numerically, estimates of the model parameters are
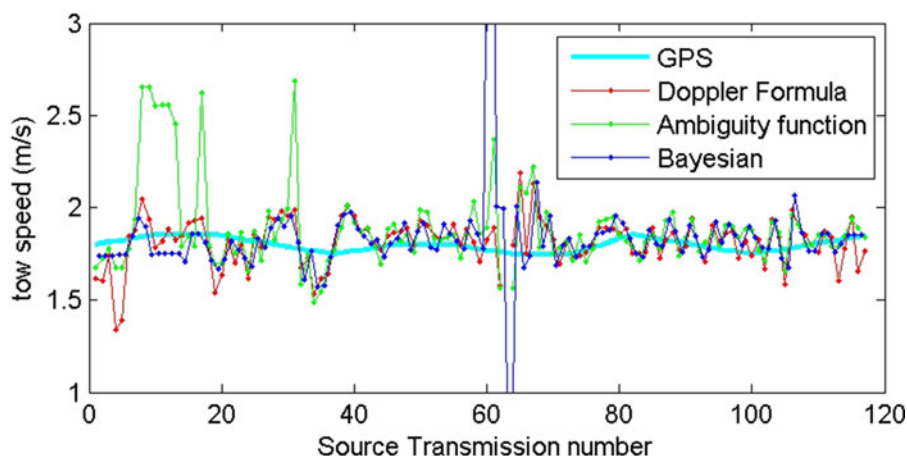
Fig. 18. Comparison of ray-based travel time geometry estimates (Bayesian) converted to ship speed Eq. (2) with other measurements, including GPS (every 5 s), and Doppler estimation using a newly derived formula [12] (every 0.5 s) and the traditional ambiguity function method. The CPA is at transmission 62.
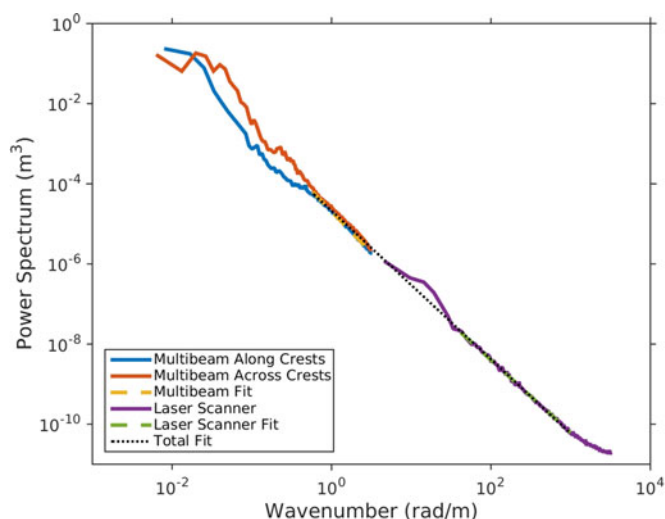

Fig. 19. Spectra of multibeam data [20] and APL-UW laser line scanner data [19] with fits.

TABLE V

MODEL PARAMETERS ESTIMATED FROM MEASURED ROUGHNESS SPECTRA FROM MULTIBEAM BATHYMETRY AND LASER LINE SCANNER DATA SCANNER IGNORING THE LOW WAVENUMBERS FROM BOTH DATA SETS

Data Source	1-D spectral strength w_1 (m^4)	1-D spectral exponent γ_1
Multibeam	2.04×10^{-5}	1.98
Laser line scanner	2.27×10^{-5}	1.86
Total	2.12×10^{-5}	1.85

very similar, although they exhibit slight discrepancies between the multibeam and line scanner measurements.

The multibeam-derived spectral parameters used in the text have Gaussian distributed interface slopes with a standard deviation of about 14°. The slope distribution is independent of the spectral cutoff values employed here, i.e., the slope distribution is dominated by the high-spatial wavenumbers. In this case

(relatively small γ), the slopes depend somewhat on the discretization. The modeling in this paper samples the boundary at 30 points per (acoustic) wavelength, thus, the 14° slopes are higher than a more typical sampling of 10 points per wavelength. Nevertheless, the 14° slopes do not seem unrealistic.

ACKNOWLEDGMENT

REFERENCES

[1] F. Jensen, W. A. Kuperman, M. B. Porter, and H. Schmidt, *Computational Ocean Acoustics*, 2nd ed. New York, NY, USA: Springer-Verlag, 2011, Sec. 2.4.3, p. 93.

[2] D. R. Jackson, R. I. Odom, M. L. Boyd, and A. N. Ivakin, "A geoacoustic bottom interaction model (GABIM)," *IEEE J. Ocean. Eng.*, vol. 35, no. 3, pp. 603–617, Jul. 2010.

[3] C. W. Holland and J. Dettmer, "In-situ sediment dispersion estimates in the presence of discrete layers and gradients," *J. Acoust. Soc. Amer.*, vol. 133, pp. 50–61, 2013.

[4] C. W. Holland, P. L. Nielsen, J. Dettmer, and S. E. Dosso, "Resolving meso-scale seabed variability using reflection measurements from an autonomous underwater vehicle," *J. Acoust. Soc. Amer.*, vol. 131, pp. 1066–1078, 2012.

[5] C. W. Holland and J. Osler, "High resolution geoacoustic inversion in shallow water: A joint time and frequency domain technique," *J. Acoust. Soc. Amer.*, vol. 107, pp. 1263–1279, 2000.

[6] J. Dettmer, S. E. Dosso, and C. W. Holland, "Trans-dimensional geoacoustic inversion," *J. Acoust. Soc. Amer.*, vol. 128, pp. 3393–3405, 2011.

[7] C. W. Holland, J. Dettmer, and S. E. Dosso, "Remote sensing of sediment density and velocity gradients in the transition layer," *J. Acoust. Soc. Amer.*, vol. 118, pp. 163–177, 2005.

[8] J. Dettmer, C. W. Holland, and S. E. Dosso, "Resolving lateral seabed variability by Bayesian inference of seabed reflection inversions," *J. Acoust. Soc. Amer.*, vol. 126, pp. 56–69, 2009.

[9] J. A. Goff, "Seismic and core investigation off Panama city, Florida, reveals sand ridge influence on formation of the shoreface ravinement," *Continental Shelf Res.*, vol. 88 , pp. 34–46, 2014.

[10] J. Goff, Unpublished notes from a seismic reflection and coring campaign along the main reverberation line.

[11] C. W. Holland, "Seabed reflection measurement uncertainty," *J. Acoust. Soc. Amer.*, vol. 114, pp. 1861–1873, 2003.

[12] S. Pinson and C. W. Holland, "Relative velocity measurement from the spectral phase of a match-filtered linear frequency modulated pulse (EL)," *J. Acoust. Soc. Amer.*, vol. 140, pp. 191–196, 2016.

[13] R. T. Bachman, "Acoustic and physical property relationships in marine sediment," *J. Acoust. Soc. Amer.*, vol. 78, pp. 616–621, 1985.

[14] J. Dettmer, S. E. Dosso, and C. W. Holland, "Model selection and Bayesian inference for high resolution seabed reflection inversion," *J. Acoust. Soc. Amer.*, vol. 125, pp. 706–716, 2009.

[15] S. Pinson, J. Cordioli and L. Guillon, "Spherical wave reflection in layered media with rough interfaces: Three dimensional modeling," *J. Acoust. Soc. Amer.*, vol. 140, pp. 1108–1115, 2016.

[16] C. A. Langston, "The effect of planar dipping structure on source and receiver responses for constant ray parameter," *Bull. Seismological Soc. Amer.*, vol. 67, no. 4, pp. 1029–1050, 1977.

[17] E. Bossy, "SimSonic suite user's guide for SimSonic2D," 2012. [Online]. Available: http://www.simsonic.fr/(07/30/2013)

[18] T. Hefner and D. J. Tang, "Seafloor laser scanner measurements at TREX13."

[19] M. Vercammen, "The reflection of sound by curved surfaces," in *Proc. Acoust.*, Paris, France, 2008, pp. 3473–3478.

[20] C. de Moustier and B. J. Kraft, "Bathymetry and 400-kHz seafloor acoustic backscatter imagery offshore," Panama City Beach, FL, USA.

[21] S. E. Dosso and G. R. Ebbeson, "Array element localization accuracy and survey design," *Can. Acoust.*, vol. 34, pp. 3–14, 2006.

Chad M. Smith (M'09) received the B.S. degree in electrical engineering technology from the Pennsylvania College of Technology, Williamsport, PA, USA, in 2006 and the M.S. degree in acoustics from The Pennsylvania State University, University Park, PA, USA, in 2010, where he is currently working toward the Ph.D. degree in acoustics.

He is a Senior Research Assistant for the Applied Research Laboratory, The Pennsylvania State University. From 2008 to 2010, he was a Graduate Research Assistant for the Applied Research Laboratory, The Pennsylvania State University. From 2006 to 2008, he was an Electrical Engineer for QorTek, Inc., Williamsport, PA, USA. His research interests include underwater and atmospheric acoustic propagation, array and transducer technology, and signal processing.

Mr. Smith is a member of the Acoustical Society of America.

Charles W. Holland received the B.S. degree in engineering from the University of Hartford, West Hartford, CT, USA, in 1983 and the M.S. and Ph.D. degrees in acoustics from the Pennsylvania State University, State College, PA, USA, in 1985 and 1991, respectively. His Ph.D. dissertation addressed acoustic propagation through and interface waves in poro-viscoelastic marine sediments.

From 1985 to 1996, he conducted research in sediment acoustic modeling and seafloor classification techniques at Planning Systems, Inc. In 1996, he joined the NATO Undersea Research Centre, La Spezia, Italy, where he developed seabed reflection and scattering measurement and parameter estimation techniques. In 2001, he joined the Applied Research Laboratory at the Pennsylvania State University where he continues his research in both theoretical and experimental aspects of ocean waveguide and seafloor acoustics.

Dr. Holland is a Fellow of the Acoustical Society of America.

Paul C. Hines received the B.Sc. degree (honors) in engineering-physics from Dalhousie University, Halifax, NS, Canada, in 1981 and the Ph.D. degree in physics from the University of Bath, Bath, U.K., in 1988.

He joined Defence R&D Canada, Dartmouth, NS, Canada, in 1981. His research on acoustic scattering from ocean boundaries earned him the Chesterman Medal from the University for "Outstanding Research in Physics." From his return to DRDC in 1988 until his departure in March 2014, he led several groups and managed a variety of acoustic research projects for both DRDC and the US Office of Naval Research. He is a Seasoned Experimentalist and has been the Chief Scientist for several collaborative international research trials. He is currently the President of Hines Ocean S&T, Inc., in addition to conducting research in the Department of Electrical and Computer Engineering and Department of Oceanography, Dalhousie University, Halifax, NS, Canada. During his career, he has conducted research in antisubmarine warfare, mine and torpedo countermeasures, rapid environmental assessment, acoustic scattering, sound-speed dispersion, vector sensor processing, sonar classification and tracking, continuous active sonar, and the application of aural perception in humans, to target classification in sonar.

Dr. Hines is a Fellow of the Acoustical Society of America, and a Distinguished Lecturer of the IEEE Ocean Engineering Society.

Samuel Pinson received the Engineer's degree in acoustics and vibration from ENSIM, Le Mans, France, in 2007, the M.S. degree in mechanics and acoustics from the Universié du Maine, Le Mans, France, in 20017, and the Ph.D. degree in underwater acoustics from the Université de Bretagne Occidentale, Brest, France, in 2011.

In summer 2012, he was a Visiting Researcher at the Center for Maritime Research and Experimentation, La Spezia, Italy. Between 2012 and 2013, he was a Postdoctoral Researcher at the Applied Research Laboratory of the Pennsylvania State University, State College, PA, USA. Between 2014 and 2016, he was a Postdoctoral Researcher at the Universidade Federal de Santa Catarina, Floriaónopolis, Brazil. His research interests include wave propagation in complex media and signal processing.

Derek R. Olson received the A.B. degree (*cum laude*) in physics from Vassar College, Poughkepsie, NY, USA, in 2009 and the Ph.D. degree in acoustics from The Pennsylvania State University, University Park, PA, USA, in 2014.

He is currently a Research Associate at the Applied Research Laboratory, The Pennsylvania State University. He was a National Defense Science and Engineering Graduate Fellow. His research concerns theoretical, numerical, and experimental investigation of acoustical scattering from ocean boundaries.

Dr. Olson is a member of the Acoustical Society of America, the IEEE Oceanic Engineering Society, Phi Beta Kappa, and Sigma Xi.

Stan E. Dosso received the B.Sc. degree in physics and applied mathematics and the M.Sc. degree in physics from the University of Victoria, Victoria, BC, Canada, in 1982 and 1985, respectively, and the Ph.D. degree in geophysics from the University of British Columbia, Vancouver, BC, Canada, in 1990.

From 1990 to 1995, he was in Ocean Physics (Arctic Acoustics) at the Defence Research Establishment Pacific, Victoria, BC, Canada. In 1995, he was appointed to an Ocean Acoustics Research Chair in the School of Earth and Ocean Sciences, University of Victoria, where he is currently a Professor and the Director of the School. His research interests involve probabilistic inverse problems in ocean acoustics and geophysics.

Dr. Dosso is a Fellow of the Acoustical Society of America and a member of the Canadian Acoustical Association (President 2003–2007) and the American Geophysical Union.

Jan Dettmer received the Diplom Geophysiker degree in geophysics from the University of Hamburg, Hamburg, Germany, in 2002 and the Ph.D. degree in earth and ocean science from the University of Victoria, Victoria, BC, Canada, in 2007.

He was with the Office of Naval Research and a Postdoctoral Fellow in 2007 and 2008, a Research Scientist at the University of Victoria from 2009 to 2013, and a Research Fellow at Australian National University from 2013 to 2016. Since 2016, he has been an Assistant Professor of Geophysics at the University of Calgary, Calgary, AB, Canada. His research interests include seismology and acoustics, in particular earthquake sources, earth structure, seabed structure, inverse problems, and uncertainty quantification.